Observational constraints on evolution of dust disc properties in Upper Scorpius

Pinilla, P.; Sierra, A.; Kurtovic, N.T.; Anania, R.; Andrews, S.; Carpenter, J.; ... ; Zhang, K.

Monthly Notices of the ROYAL ASTRONOMICAL SOCIETY

MNRAS **543,** 2723–2743 (2025) https://doi.org/10.1093/mnras/staf1624
Advance Access publication 2025 September 25

Observational constraints on evolution of dust disc properties in Upper Scorpius

Paola Pinilla [1]★ Anibal Sierra [1]† Nicolas T. Kurtovic,[2] Rossella Anania,[3] Sean Andrews,[4] John Carpenter,[5] Osmar Guerra-Alvarado,[6] Feng Long,[7]‡ Sebastian Marino [8] Miguel Vioque[9] and Ke Zhang[10]

[1]*Mullard Space Science Laboratory, University College London, Holmbury St Mary, Dorking, Surrey RH5 6NT, UK*
[2]*Max Planck Institute for Extraterrestrial Physics, Giessenbachstrasse 1, D-85748 Garching, Germany*
[3]*Dipartimento di Fisica, Università degli Studi di Milano, Via Celoria 16, I-20133 Milano, Italy*
[4]*Center for Astrophysics, Harvard & Smithsonian, 60 Garden St., Cambridge, MA 02138, USA*
[5]*Joint ALMA Observatory, Avenida Alonso de Córdova 3107, Vitacura 19001, Santiago, Chile*
[6]*Leiden Observatory, Leiden University, PO Box 9513, 2300 RA Leiden, the Netherlands*
[7]*Lunar and Planetary Laboratory, The University of Arizona, Tucson, AZ 85721, USA*
[8]*School of Physics and Astronomy, University of Exeter, Astrophysics Group, Stocker Road, Exeter EX4 4QL, UK*
[9]*European Southern Observatory, Karl-Schwarzschild-Str. 2, D-85748 Garching bei München, Germany*
[10]*Department of Astronomy, University of Wisconsin-Madison, 475 N Charter St, Madison, WI 53706, USA*

Accepted 2025 September 22. Received 2025 September 18; in original form 2025 July 23

ABSTRACT

Protoplanetary discs in the Upper Scorpius star-forming region are excellent laboratories to investigate late stages of planet formation. In this work, we analyse the morphology of the dust continuum emission of 121 discs from an Atacama Large Millimeter Array (ALMA) Band 7 survey of the Upper Scorpius region. This analysis is done in the visibility plane, to measure the flux, geometry and characterize potential structures. We compare the results with state-of-the art gas and dust evolution models that include external photoevaporation, with mild values of the $F_{\rm UV}$ of 1–40 G_0. From the visibility analysis, 52 of the 121 discs are resolved (43 per cent). From the resolved discs, 24 discs have structures and 28 remain as smooth discs at the mean resolution scale of ∼0.1 arcsec (∼14 au). Our results show no significant dust disc size evolution of the surviving discs in UpperSco when compared to discs in younger star-forming regions, such as Lupus. We find a strong, steeper-than-previously-reported correlation between dust disc size and disc millimetre continuum luminosity, in agreement with drift-dominated dust evolution models. We also find positive correlations between the dust disc mass versus stellar mass and dust disc size versus stellar mass. The slope of the dust disc size versus stellar mass relationship is steeper compared to younger star forming regions. Additionally, we observe no significant correlation between dust disc properties and the environmental $F_{\rm UV}$, consistent with models predicting that dust disc properties are primarily shaped by drift and dust traps. Our models predict that gas disc masses and sizes should be highly affected by the moderate $F_{\rm UV}$ values that Upper Scorpius discs experience in contrast to the dust. This highlights the need for deeper and higher-resolution ALMA observations of gas in these discs exposed to mild external photoevaporation to further constrain their evolution and fate.

Key words: protoplanetary discs.

1 INTRODUCTION

The discovery and characterization of exoplanets over the past decades have revealed a remarkable diversity of planetary systems (J. N. Winn & D. C. Fabrycky 2015; J. J. Lissauer, N. M. Batalha & W. J. Borucki 2023; D. Valencia, A. Moro-Martin & J. Teske 2025). A key challenge is to determine the processes that govern the chemical and physical evolution of protoplanetary discs – the birthplaces of planets – during planet formation. Demographic observations of protoplanetary discs that span a large range of ages and under different conditions are crucial to investigate the overall trends of disc properties, such as gas and dust mass/sizes.

In the last decade, observations from the Atacama Large Millimeter Array (ALMA) have provided insights into the evolution of the disc properties, in particular of the dust disc mass and size (e.g. M. Ansdell et al. 2016; S. A. Barenfeld et al. 2016; L. A. Cieza et al. 2019), which has been used to compare with gas and dust evolution models to understand the physical process that dominate the evolution (e.g. G. P. Rosotti et al. 2019; P. Pinilla, I. Pascucci

★ E-mail: p.pinilla@ucl.ac.uk
† The first and second authors of this paper equally contributed to this work.
‡ NASA Hubble Fellowship Program Sagan Fellow

& S. Marino 2020; C. Toci et al. 2021; A. Zormpas et al. 2022). Understanding the evolution of discs from early phases when they are still embedded (Class 0/I discs) to later stages, including the latest stages before the gas disc fully dispersed, is crucial to understand the overall picture of planet formation.

The Upper Scorpius star-forming region (hereafter UpperSco) is often considered a standard reference for studying the later stages of the gas disc phase in protoplanetary disc evolution, as it has several populations with ages ranging from ∼3 and 10 Myr old (or even older e.g. M. J. Pecaut, E. E. Mamajek & E. J. Bubar 2012; K. L. Luhman & T. L. Esplin 2020; J. J. Armstrong et al. 2025), which corresponds to the late stages of disc evolution (e.g. D. Fedele et al. 2010). The disc millimetre fluxes are known to be lower in UpperSco in comparison to younger star forming regions (S. A. Barenfeld et al. 2016; I. Pascucci et al. 2016; M. Ansdell et al. 2017; J. M. Carpenter et al. 2025). In addition, the dust disc size seems to be smaller as well, as suggested by N. Hendler et al. (2020).

However, only recently a comprehensive picture of the gas disc evolution has been done, albeit with only few discs. The large ALMA program AGE-PRO aimed to analyse the gas evolution of protoplanetary discs by observing 30 protoplanetary discs in three different star forming regions: Ophiuchus, Lupus, and UpperSco, representing three different stages of disc evolution. The stellar spectral type in this sample was restricted to be between M3-K6, in order to have a narrow dependence with stellar type (K. Zhang et al. 2025). Two of the conclusions of the AGE-PRO collaboration are: (1) the median gas mass of the young discs (<1 Myr) is one order of magnitude higher than in the Lupus and UpperSco, while there is not a significant difference between the gas mass of the Lupus and UpperSco surviving discs (L. Trapman et al. 2025a); (2) the median gas disc size obtained from the ^{12}CO observations slightly increases from Lupus to UpperSco (L. Trapman et al. 2025b). Both of these results are interesting, partially because the discs in UpperSco are subject to mild external photoevaporation by $F_{\rm UV}$ radiation from OBA-type stars in the association, which can reduce the gas disc mass and truncate the disc efficiently (R. Anania et al. 2025a). This challenges the comparison with younger star forming regions that have lower $F_{\rm UV}$ irradiation fields.

In this study, we analyse continuum observations from the ALMA survey of UpperSco conducted by J. M. Carpenter et al. (2025). Compared to N. Hendler et al. (2020), we increase the sample from 22 discs to 121 discs, with a resolution that it is in average three times higher. The analysis is performed in the visibility domain to derive dust disc fluxes, sizes, and inclinations. For a subset of the UpperSco sample, we incorporate gas disc sizes derived by Zagaria et al. (in preparation) to quantify dust–gas size ratios. We also compare the observations to disc models that include external photoevaporation, focusing on how FUV radiation fields typical of UpperSco influence disc sizes and structures.

This paper is organized as follows. Section 2 explains the sample and procedure of the modelling of the data in the visibility plane. Section 3 summarizes the gas and dust evolution models of this work, in addition to initial conditions. Moreover, we explain in this section how different observables are calculated from the models in order to compare with ALMA data. Section 4 includes all the results from the observations and models. Sections 5 and 6 present the discussion and conclusions of our work, respectively.

2 SAMPLE AND VISIBILITY MODELLING

The data used in this work correspond to observations taken with ALMA in Band 7 (0.88 mm) to detect the dust continuum and the CO J=3-2 (J. M. Carpenter et al. 2025). The spectral windows of these observations were centred at 334.2, 336.1, 346.2, and 348.1 GHz, with a bandwidth of 1.875 GHz for each window. A total of 121 discs confirmed as members of UpperSco were detected in dust continuum emission with a signal-to-noise-ratio (SNR) > 3, and 83 of these were also detected in CO with a SNR > 5. The resolution of these observations is between 0.1–0.3 arcsec, with a typical on-source integration time of 2.5 min, which provides a sensitivity of the dust continuum emission of 0.15 mJy beam^{-1}.

We use GALARIO (M. Tazzari, F. Beaujean & L. Testi 2018) to model the dust continuum visibilities of 121 discs in UpperSco and constrain their flux, size, and geometry. We assume axisymmetric discs, and an intensity radial profile described by a Gaussian function. The amplitude (f_0), width (σ_r), and radial peak position ($R_{\rm peak}$) of the Gaussian are free parameters of the fit. This model allows for the description of both smooth and ringed discs. In addition, the disc inclination (inc), position angle (PA), and offset from the phase centre (dRA, dDec) are also fitted for each disc, resulting in a total of seven free parameters.

This model is initially tested for all discs. However, the geometry and size (defined as the location where either 68 per cent or 90 per cent of the total flux is enclosed) of some faint and compact discs are not well constrained as the corresponding fits do not converge. In such cases, the brightness is modelled as a point source (a delta function δ) with a total flux $F_{340\,\rm GHz}$ and at position (dRA, dDec) relative to the phase centre. The Fourier transform of the point source is not computed with GALARIO, but directly from

$$\mathcal{F}[F_{340\,\rm GHz}\delta(\alpha_{\rm RA}-{\rm dRA},\ \beta_{\rm Dec}-{\rm dDec})] = \times F_{340\,\rm GHz}\exp(-2\pi i(u\,{\rm dRA}+v\,{\rm dDec})), \quad (1)$$

where $\alpha_{\rm RA}$ and $\beta_{\rm DEC}$ are the right ascension and declination coordinates, respectively, and u and v are the spatial frequencies in the Fourier domain (uv-distances). Since the discs are unresolved in this model, their geometry remains unconstrained, and their size upper limit is given by an angular resolution of 0.1 arcsec (14.5 au at an average distance of 145 pc for the discs in UpperSco). A total of three free parameters (flux and offsets) are fitted for the unresolved discs.

In both cases (resolved and unresolved), the parameter space is explored using a Markov Chain Monte Carlo (MCMC), as implemented in the PYTHON library EMCEE (D. Foreman-Mackey et al. 2013). The number of walkers per free parameter is set to 8. For resolved discs, the image models are generated with a resolution of 256 × 256 pixels and a pixel size of 0.02 arcsec. The prior for each parameter follows a uniform distribution. The number of steps is set to 30 000, which was found to be sufficient for parameter convergence. A final run of 10 000 steps is performed to estimate the parameters and their uncertainties.

Tables A1 and A2 present stellar and disc parameters obtained in this study, and in Section 4.1 we present and discuss the normalized intensity profiles of the resolved discs. We classify the resolved discs into two categories: structured discs and smooth discs. The former are defined as those in which the peak of the best-fitting Gaussian function is resolved ($R_{\rm peak} > 0.05$ arcsec), while in the latter, it remains unresolved ($R_{\rm peak} \leq 0.05$ arcsec). The value of 0.05 arcsec is chosen as an average value of the half of the beam size of the observations for the sample (J. M. Carpenter et al. 2025), and it is a conservative choice, as the typical resolution reached in the visibility analysis is finer (A. Sierra et al. 2024). It is important to note that in none of the clean images prominent multiple rings or more complex structures were clearly identified at the current resolution, justifying the choice of a single Gaussian, but with this approach we may still

miss some structures as faint rings/gaps, azimuthal asymmetries, or small cavities.

3 MODELS

3.1 Gas and dust evolution models

To perform the gas and dust evolution models of this work, we use the 1D code DUSTPY (S. M. Stammler & T. Birnstiel 2022), version 1.0.5. DUSTPY is a publicly available code that follows the dynamics and growth of dust particles simultaneously in the radial direction in protoplanetary discs, while the gas evolves by viscous evolution. To include external photoevaporation by ultraviolet (UV) radiation from nearby massive stars, we follow the prescription implemented by M. Gárate et al. (2024) in DUSTPY. For this implementation, the gas surface density loss rate is calculated from the FRIED grid from T. J. Haworth et al. (2018), and for the loss of dust particles that are entrained by the photoevaporative wind we use the models by A. D. Sellek, R. A. Booth & C. J. Clarke (2020). We used an updated version of the FRIED grid (T. J. Haworth et al. 2023), as implemented in DUSTPY in R. Anania et al. (2025a).

Based on the properties of the UpperSco discs (J. M. Carpenter et al. 2025), we performed simulations for two different types of stars: a solar type star with a stellar mass of 1.0 $M_\odot$ and a luminosity of 1.0 $L_\odot$; and an M-dwarf with a stellar mass of 0.3 $M_\odot$ and a luminosity of 0.3 $L_\odot$. In the sample of J. M. Carpenter et al. (2025), most of the discs are around M3–M5 stars, so our second choice is more representative when we compare to the data.

The gas surface density is assumed to be a power law with an exponential cut-off (D. Lynden-Bell & J. E. Pringle 1974), that is,

$$\Sigma_g(r) = \Sigma_0 \left(\frac{r}{r_c}\right)^{-\gamma} \exp\left[-\left(\frac{r}{r_c}\right)^{2-\gamma}\right], \quad (2)$$

and we assume the cut-off radius r_c to be 80 au, and $\gamma = 1$. The initial disc mass is $M_{disc} = 0.05\, M_\star$, which sets the value of Σ_0 for each of the stellar masses assumed in this work. Although the value of r_c is large compared to values obtained from observations (L. Trapman et al. 2025b), R. Anania et al. (2025a) and N. T. Kurtovic et al. (2025) showed that varying r_c has low influence on the gas and dust evolution over million year time-scales. We chose $r_c = 80$ au to allow that the assumed traps are able to keep dust particles in the outer disc over million years of evolution, as traps assumed outside r_c trap very little dust available in the outer disc (M. Gárate et al. 2024).

For the disc temperature, we assume only the stellar irradiation (S. J. Kenyon & L. Hartmann 1987). The radial grid in our simulations is from 1 to 300 au with 150 grid cells, which is logarithmically spaced. For some of our simulations, we perform resolution tests with a double number of cells, resulting in no differences on the final disc properties and evolution. For the dust grain size distribution $n(a)$, we assume that it is initially distributed as a power law as $n(a) \propto a^{-3.5}$ (with a being the grain size) from 0.5–1 μm. The exponent of −3.5 is assumed as the value from the size distribution of interstellar grains (J. S. Mathis, W. Rumpl & K. H. Nordsieck 1977). The grain size grid is logarithmically spaced, and it spans from 0.5 μm to 25 cm, with cells. The initial dust-to-gas ratio is assumed to be as the interstellar medium, with a value of 1/100. The grains in the simulations are allowed to grow and fragment. Particles fragment when they reach a threshold in their relative velocities, which is called the fragmentation velocity, and it is assumed in this work to be constant and equal to 10 m s^{-1}, as typically assumed for water-ice particles (e.g. B. Gundlach & J. Blum 2015)

Table 1. Parameter space of the gas and dust evolution models.

Quantity/Unit	Description	Value
$M_\star[M_\odot]$	Stellar mass	0.3, 1.0
$T_\star$[K]	Stellar effective temperature	3000, 5772
$L_\star[L_\odot]$	Stellar luminosity	0.3, 1.0
r_{in} [au]	Inner radial boundary	1.0
r_{out} [au]	Outer radial boundary	300
r_c [au]	Cut-off radius	80
n_r	Number of radial cells	150
M_{disc} $[M_\star]$	Disc mass	0.05
α_0	Disc viscosity	10^{-3}
v_f [m s^{-1}]	Fragmentation velocity	10
ρ_s[g cm^{-3}]	Grain material density	1.7
A	Amplitude of pressure bumps	0, 1, 4, 50
r_{gap} [au]	Location of gaps for $A = 1, 4$	10, 40, 70
r_{gap} [au]	Location of gap for $A = 50$	40
F_{UV} $[G_0]$	External UV flux	1, 10, 20, 40

We explored four values of F_{UV}, that is, 1, 10, 20, and 40 G_0; based on the calculations in Zagaria et al. (in preparation) for the sources used in this work in UpperSco. We turn-on the effect of external photoevaporation at 1 Myr of evolution, as we assume that at early ages the discs could have been shielded by the envelope (L. Qiao et al. 2022). R. Anania et al. (2025a) demonstrated that the assumption of turning-on external photoevaporation later in the disc evolution does not change the results at longer times, because in this case the disc properties rapidly evolve to the same values as if external photoevaporation would be active from the beginning of the simulation.

We include the presence of pressure bumps in our models, by adding a perturbation to the viscous α_{visc} profile, which creates a gap-like structure in the gas surface density profile, as in J. Stadler et al. (2022), M. Gárate et al. (2024) and N. T. Kurtovic et al. (2025). The perturbation in the α profile has the shape of a Gaussian bump, that is,

$$\alpha_{visc}(r) = \alpha_0 \left(1 + A \exp\left(-\frac{(r - r_{gap})^2}{2w_{gap}^2}\right)\right), \quad (3)$$

where α_0 is the global viscous disc parameter (N. I. Shakura & R. A. Sunyaev 1973) that is assumed to be 10^{-3} for all simulations. A sets the strength of the pressure bumps, and it is taken to be $A = 0, 1, 4, 50$, where $A = 1, 4$ represents weak and strong pressure bumps, respectively, as implemented in P. Pinilla et al. (2020). In the case of $A = 1$ and $A = 4$, there are three bumps or gaps considered simultaneously in the disc and centred at $r_{gap} = 10, 40, 70$ au, all of them with a width w_{gap} equal to the local pressure scale height. The number and location of the traps is motivated by observations of protoplanetary discs. In the compilation of discs by J. Bae et al. (2023) most of the observed rings have been found between 20–80 au. The case of $A = 50$ is assumed to mimic a very deep gap as observed in discs with large cavities, the well-known transition discs (hereafter transition disc-type trap). In this case, only one gap is considered at $r_{gap} = 40$ au, with a width equal to three scale heights. We run the simulations from 0–10 Myrs, saving a total of 12 snapshots at $t_{snapshots} = [0.001, 0.005, 0.01, 0.05, 0.1, 0.5, 1, 2, 3, 5, 7, 10]$ Myr. All the model parameters are summarized in Table 1.

3.2 Synthetic observable properties

To compare with the ALMA observations, we calculate different observable properties using the dust size distribution obtained for each snapshot of the DUSTPY simulations. These dust distributions are used to calculate the optical depth at each radius $\tau_\nu(r)$ with $\nu = 340$ GHz as

$$\tau_\nu(r) = \frac{\sum_a \kappa_\nu(a)\,\sigma(a,r)}{\cos i}, \tag{4}$$

where $\sigma(a,r)$ is the vertically integrated dust surface density and $\kappa_\nu(a)$ are the dust opacities, for which the dust composition is assumed to be as in L. Ricci et al. (2010), but for compact grains. The disc inclination is assumed to be $i = 45^\circ$.

For the calculation of the flux at 340 GHz (880 mm), we assume for simplicity only thermal emission from the dust, so the intensity as a function of radius is given by,

$$I_\nu(r) = B_\nu(T(r))\left[1 - \exp(-\tau_\nu(r))\right], \tag{5}$$

where $B_\nu(T)$ is the Planck function at a temperature of $T(r)$. While in the models, the gas and dust have the same temperature (T_g), for the calculation of the disc observables, we assume there is a background temperature of $T_\mathrm{b} = 20$ K, to account for the irradiation from other stars in the region as in M. Gárate et al. (2024), this means that

$$T(r) = \sqrt[4]{T_\mathrm{g}(r)^4 + T_\mathrm{b}^4}. \tag{6}$$

The intensity profile is convolved with a Gaussian beam of size 0.1 arcsec, to account for a similar resolution of the UpperSco observations. The total flux is calculated as $F_\nu = \int I_\nu \,\mathrm{d}\Omega$, where $\mathrm{d}\Omega$ is the solid angle covered by the disc in the sky, assuming a distance of 145 pc.

The dust disc radius is defined as the location that encloses 90 per cent of the flux (R_{90}). For this, we assume a sensitivity 0.15 mJy beam^{-1}, similar to the value of the observations (J. M. Carpenter et al. 2025). This means that in our calculations, any value of the flux lower than three times this sensitivity threshold is assumed as a non detection.

In addition, we calculate the gas disc size from the models as the location that encloses 90 per cent of ^{12}CO line flux (hereafter, R_CO). To obtain this location, we assume the analytical prescriptions in L. Trapman et al. (2023). They used thermochemical models to find an empirical correlation between the gas column density at the observed gas disc size R_CO and the mass of the disc, which does not significantly depend on other disc parameters. This column density is

$$N_\mathrm{gas}(R_\mathrm{CO}) \approx 10^{21.27-0.53\log(L_\star)} \left(\frac{M_\mathrm{gas}}{\mathrm{M}_\odot}\right)^{0.3-0.08\log(L_\star)}, \tag{7}$$

where $L_\star$ is the stellar luminosity and M_gas is the gas disc mass. The R_CO value is then calculated when $\Sigma_g(R_\mathrm{CO}) = N_\mathrm{gas}(R_\mathrm{CO})\mu_\mathrm{gas}$, with μ_gas being 2.3 μ_H (μ_H is the mass of atomic hydrogen). It is worth noticing that the background temperature added in equation (6) does not affect the calculation of $N_\mathrm{gas}(R_\mathrm{CO})$ in equation (7).

4 RESULTS

4.1 Intensity profiles and dust disc size

From the analysis in the visibility plane of the entire sample, we find that 24 discs (∼20 per cent) are resolved and structured, 28 (∼23 per cent) are resolved and remain smooth at the current resolution; and 69 (∼57 per cent) are unresolved. Fig. 1 shows the ALMA images (top panels) and the the model images from the visibility fitting (bottom panels) for all the resolved discs in the sample. The total flux of each disc is given in the individual panels of the images from the visibility fitting. In addition, Fig. 2 shows the best intensity profile (normalized to the peak) for each of the discs that are resolved (top panels). The vertical lines in this figure correspond to the position of R_{90}, which is the location that encloses 90 per cent of the total continuum flux. The bottom panels of Fig. 2 are the real part of the binned visibilities, with the best-fitting model overplotted. In this paper, we also use R_{68}, corresponding to the location that encloses 68 per cent of the total flux, commonly used in previous papers (e.g. A. Tripathi et al. 2017; S. M. Andrews et al. 2018; N. Hendler et al. 2020; N. T. Kurtovic et al. 2021; M. Vioque et al. 2025). Fig. B1 in the Appendix shows the fluxes, dust disc sizes, and inclinations of the fit in comparison with the values reported in J. M. Carpenter et al. (2025) and Zagaria et al. (in preparation), showing in general good agreements. It is worth noting that for all the figures in this work, we use the values obtained from the visibility modelling for the dust disc sizes only for the resolved discs. For the unresolved discs, the disc size upper limit is given by an average of the beam size in the image plane. For the fluxes reported in figures, we use the values of the visibility fitting for the resolved discs, while for the unresolved discs we use the values from J. M. Carpenter et al. (2025), as their typical uncertainties are lower. This is because in our visibility fitting, we do not impose a zero offset, so the point source model can wander to noise peaks. The values for the stellar and disc properties obtained in this work are summarized in Tables A1 and A2.

Fig. 3 shows the distribution of R_{90} (left) and R_{68} (right) inferred from dust continuum visibility modelling for discs with structures (blue), smooth discs (orange), and all resolved discs (black). The discs that are unresolved are not included. The vertical line indicates the median value of each distribution, which are summarized in Table 2. We compare the cumulative distribution function (CDF) of smooth versus the structured discs using the two-sample Kolmogorov–Smirnov test (K–S test), and we find that these two distributions are significantly different. Fig. 4 shows the distribution of unresolved, structured, and smooth discs according to spectral type. This histogram shows that unresolved discs are more commonly found around later-type stars.

The rate of discs that have been classified as structured with a comparable resolution (∼0.1 arcsec) is similar than in Taurus (30 per cent; F. Long et al. 2019), which is a younger star-forming region (∼1–3 Myr) than UpperSco. The analysis in F. Long et al. (2019) was limited to 30 discs, which stellar types are earlier than M2. As it is shown in Fig. 4 the rate of structured discs in our UpperSco sample decreases for late M-dwarfs. For discs around K-, M0-, and M1-stars, the structured discs rate ranges between ∼50–60 per cent, and it decreases to 20 per cent for M2 and M3. A follow-up study of the same Taurus sample from F. Long et al. (2019) revealed additional compact or smooth discs with structures at ∼0.1 arcsec resolution, increasing the detection rate to ∼56 per cent (S. Zhang et al. 2023), which is similar to our rates for M1-K stars.

The discs in UpperSco analysed by the AGE-PRO collaboration are a subset of the analysed sample in this work, but observed at 0.2–0.3 arcsec resolution and with much higher sensitivity (C. Agurto-Gangas et al. 2025). When restricting the calculation of the median value of R_{90} and R_{68} to the same spectral type as AGE-PRO (stellar types between M3-K6), we found ∼27 au and ∼19 au, respectively, which are similar to the median values found in the AGE-PRO sample (M. Vioque et al. 2025).

O. M. Guerra-Alvarado et al. (2025) recently analysed a total of 73 discs in Lupus, covering a spectral type between M5-K2, observed

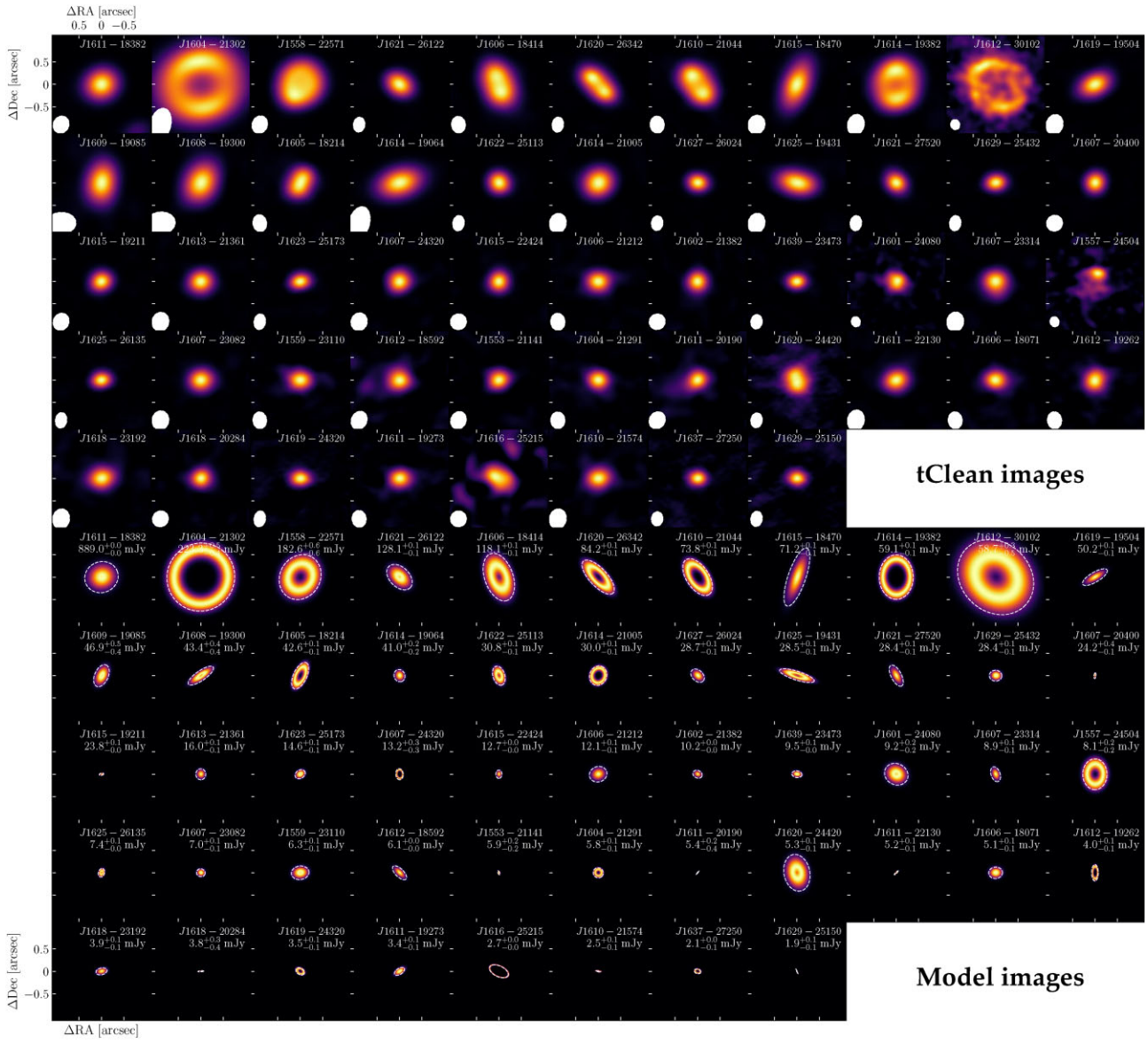

Figure 1. Gallery of the ALMA images (top panels) and the corresponding visibility modelling images (bottom panels) of the discs that are resolved, organized by millimetre brightness. Each image is normalized to the peak and shown with a linear colour stretch. In the visibility modelling images, the dashed-white lines represent R_{90}, and the total flux is given in each panel.

with ALMA at a resolution of 0.03–0.04″, and demonstrated that around 67 per cent of the discs in Lupus are smaller than 30 au (most of them around M-type stars, 73 per cent), and within that group the rate of disc with structures is similar to our rate in UpperSco (28 per cent in Lupus), while for large discs (>30 au) the large majority of discs (∼80 per cent) in Lupus have structures. We compare the distribution of the dust continuum disc radii (R_{90}) in Lupus versus UpperSco in Fig. 5, which shows the CDFs when using the total, structured, and smooth disc sample using the Kaplan–Meier estimator (as implemented in LIFELINES; C. Davidson-Pilon et al. 2019). The $p-$value obtained from the `logrank` test from LIFELINES, which includes upper limits for the unresolved discs in the total sample is reported Fig. 5. These values are higher than 1 per cent in all cases, implying that the distributions between Lupus and UpperSco remain undistinguishable and that there is no significant evolution of R_{90} between the two regions that mark different disc evolutionary stages. The median values for Lupus are summarized in Table 2.

4.2 Dust disc size versus millimetre flux

Fig. 6 shows the R_{90} (left panel) and the R_{68} (right panel) radius versus the dust continuum flux at Band 7 (340 GHz or ∼0.88 mm) normalized at 145 pc. We also show in this figure the line corresponding to an optical depth of $\tau \gg 1$ (dashed magenta line), assuming a dust temperature of 20 K. Optically thinner discs lie on the left side of this line.

To quantify a potential correlation between these quantities, we perform a Bayesian linear regression using LINMIX (B. C. Kelly 2007), such that $\log(R_{90}) = \alpha + \beta \log(F_{340\,\mathrm{GHz}})$, and similarly for R_{68}. For this fit, we include the unresolved discs (or upper limits

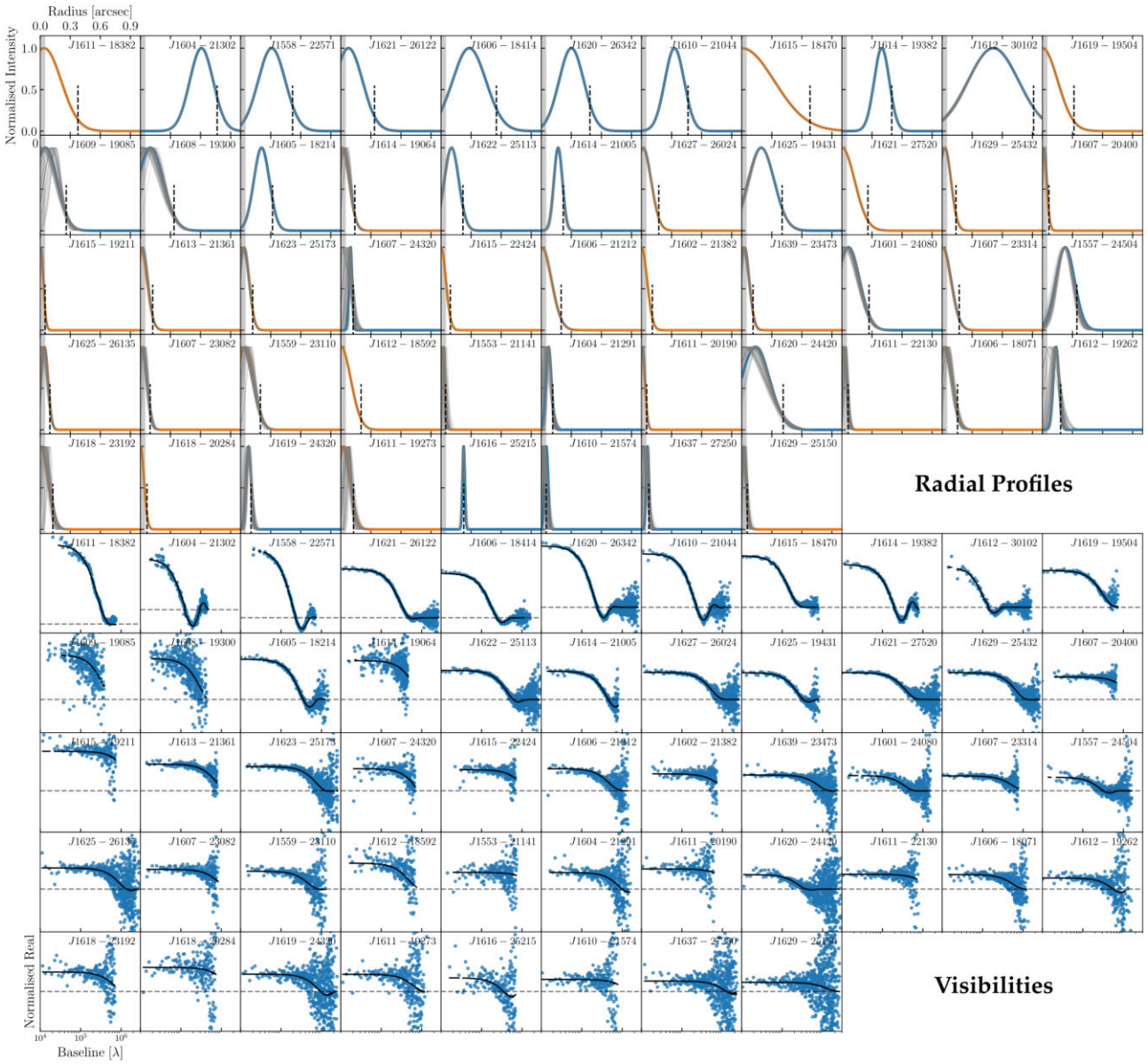

Figure 2. Upper panels: Normalized intensity radial profiles (orange for smooth discs and blue for structured discs) obtained from the visibility modelling for the resolved discs in our sample. The dashed vertical lines indicate the position of R_{90}. The grey shaded area indicates the region within 0.05 arcsec (1/2 beam size). We over-plot the last 250 models for each fit to show the typical uncertainties of the fits. Bottom panels: Real part of the visibilities, binned at 3kλ (blue points), and the best-fitting model (black lines) for all the resolved discs in the sample.

in this fit). The values for the slope and the intercept of this fit are summarized in Table 3.

In addition, we calculate the variance or the regression intrinsic scatter (σ) and the correlation coefficient (ρ), which are also reported in Table 3. Both correlations are steeper and stronger (that is, a higher correlation coefficient) than previously reported in N. Hendler et al. (2020) for UpperSco. This correlation can partially be the result of the optical depth of discs, as the $\tau \gg 1$ line in Fig. 6 suggests, which is discussed in more details in Section 5.

In N. Hendler et al. (2020), the value of the slope for the dust disc size versus luminosity relationship using a sample of 22 discs in UpperSco is much flatter (specifically: $R_{68} \propto L_{\rm mm}^{0.22}$) than we find in this study ($R_{68} \propto L_{\rm mm}^{0.68}$). N. Hendler et al. (2020) found a steeper correlation for younger star forming regions, including Ophiuchus, Taurus, Lupus, and Chamaeleon I, with slopes between 0.60–0.40. They also covered a large span of stellar masses between ∼0.08–4 $M_\odot$. In S. M. Andrews et al. (2018), an analysis of ALMA and SMA observations of 105 discs in Lupus, Taurus and Ophiuchus gave a relationship such that $R_{68} \propto L_{\rm mm}^{0.49}$.

In the analysis of O. M. Guerra-Alvarado et al. (2025) of discs in Lupus, the slope of this correlation is 0.61 ± 0.06, similar to the value reported in A. Tripathi et al. (2017), S. M. Andrews et al. (2018), and N. Hendler et al. (2020) for Lupus, which within the uncertainties is similar to the correlation found for UpperSco in this work. Therefore, we suggest that the dust disc size versus millimetre flux relationship does not show any evolutionary change when comparing younger star forming regions to UpperSco.

M. Vioque et al. (2025) performed an analysis of this correlation for the discs of the AGE-PRO sample, including 10 discs in UpperSco, which are part of the sample analysed in this work.

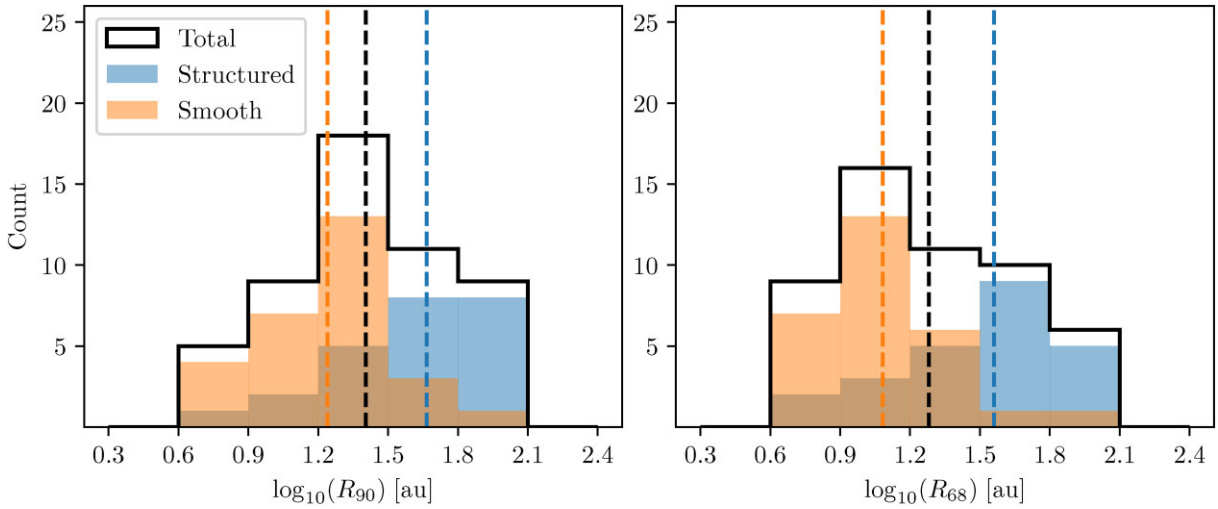

Figure 3. Distribution of R_{90} (left) and R_{68} (right) inferred from dust continuum visibility modelling for the resolved discs with structures (blue) smooth discs (orange), and all resolved discs (in black). The vertical line indicates the median value of each distribution.

Table 2. Median values of dust continuum disc radii, R_{90}.

	UpperSco R_{90} [au]	Lupus R_{90} [au]
Total	$25.4^{+10.2}_{-7.7}$	$18.5^{+6.6}_{-6.9}$
Smooth	$17.4^{+5.2}_{-4.1}$	$9.9^{+5.4}_{-3.0}$
Structured	$46.3^{+16.9}_{-15.9}$	$53.3^{+40.1}_{-28.2}$

Note. The errors correspond to the 95 per cent confidence regions (or 2σ) using the Kaplan–Meier estimator. Upper limits are included for the discs in the total sample of UpperSco and that are not resolved in this study. The Lupus values are calculated from O. M. Guerra-Alvarado et al. (2025).

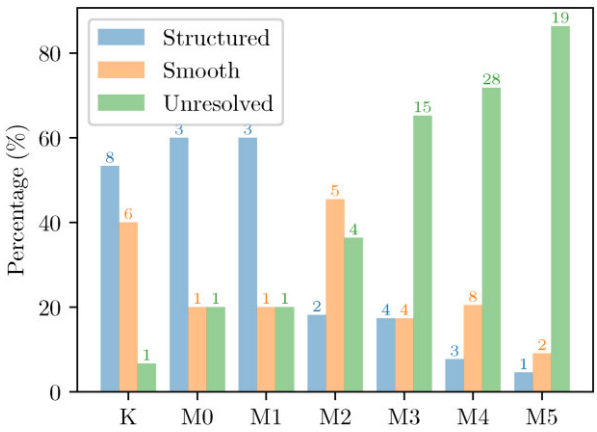

Figure 4. Distribution of unresolved, structured, and smooth discs in UpperSco based on the spectral type of the hosting star. The number of discs in each category is shown on the top of each bar.

They did not find a correlation between the dust disc size and disc luminosity. They also used the data from N. Hendler et al. (2020) sample and limited it to the AGE-PRO spectral type range and found no correlation. The correlation is found in our analysis when we restrict the stellar type as in the AGE-PRO sample, with similar values than the whole sample of the slope and intercept (Table 3), both of them with correlation coefficients that indicate a positive correlation. Therefore, when restricting the stellar type M3-K6, this correlation only becomes clear in UpperSco with the full sample analysed in this work.

In addition, we also perform the fit of the smooth and unresolved discs separately from the structured discs, finding a steeper slope for the smooth/unresolved versus structured discs (Table 3). We note that the large difference in the slope is driven by the upper limits (unresolved discs). When the upper limits are not included in the fit, the smooth and structured discs have a similar slope in the dust disc size versus millimetre flux relationship.

4.3 Gas versus dust disc size

Zagaria et al. (in preparation) measured gas disc sizes for the 78 discs in the sample of UpperSco where emission from ^{12}CO $J = 3 - 2$ was detected at $>5\sigma$ level. Zagaria et al. (in preparation) used the method introduced in L. Trapman et al. (2025b), where the gas disc size is measured from unconvolved best-fitting models to the image. From the 78 discs, $R_{\rm CO}$ could be measured in 67 discs and 11 of them only have upper limits. The top panel of Fig. 7 shows the $R_{\rm CO}$ radius obtained from the CO analysis versus the dust disc size (R_{90}) for the discs for which, both the dust continuum and the CO are detected.

The median value of the $R_{\rm CO}/R_{90}$ ratio for all the resolved discs is $2.7^{+0.3}_{-0.4}$. If the calculation is split between structured and smooth discs, the values of $R_{\rm CO}/R_{90}$ are $2.3^{+0.4}_{-0.5}$ and $4.1^{+0.5}_{-1.8}$, respectively (errors correspond to the 68 per cent confidence interval). To check if the distribution of the $R_{\rm CO}/R_{90}$ ratio is significantly different in the structured versus the smooth discs, we compare the two distributions and calculate the $p-$value from the `logrank` test from LIFELINES, finding that is much lower than 1 per cent, meaning that these two distributions are significantly different in our UpperSco sample (bottom panel of Fig. 7).

The $R_{\rm CO}/R_{90}$ ratio is in all cases higher than unity and in 10 discs is higher than 4. Ratios of $R_{\rm CO}/R_{90}$ lower than 4 can explained by the difference in optical depth between the optically thick ^{12}CO and the more optically thin continuum emission (A. Dutrey et al. 1998; S. Guilloteau & A. Dutrey 1998; S. Facchini et al. 2017). The disc with the highest $R_{\rm CO}/R_{90}$ is 2MASS-J16072955-2308221 with a value of $10.8^{+2.9}_{-3.2}$, and the disc with the lowest $R_{\rm CO}/R_{90}$ is 2MASS-J16140792-1938292 with a value of $1.1^{+0.04}_{-0.004}$. These two discs are

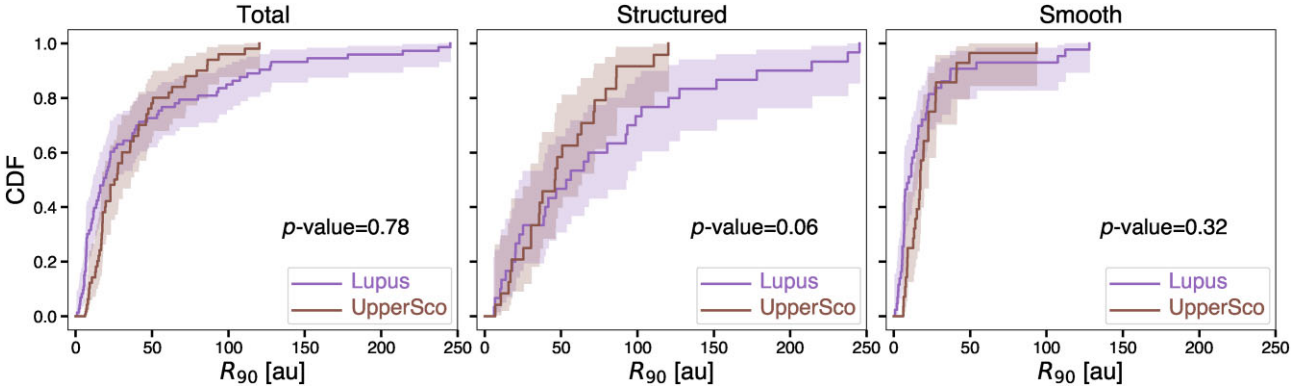

Figure 5. CDFs of the dust continuum disc radii (R_{90}) for the Lupus sample (O. M. Guerra-Alvarado et al. 2025) and the UpperSco sample of this study. Left to right panels correspond to the: total (including upper limits for the case of UpperSco), structured and smooth discs sample in each region. The panels show the $p-$values, which are higher than 1 per cent in all cases, implying that the two distributions remain undistinguishable.

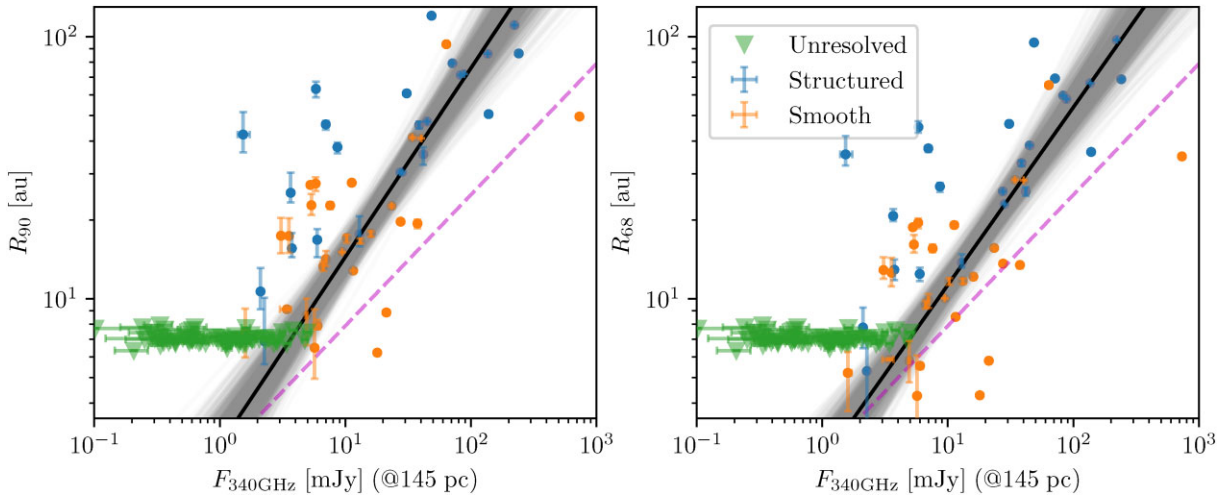

Figure 6. R_{90} (left panel) and R_{68} (right panel) versus the dust continuum flux at Band 7 normalized at 145 pc. Blue and orange dots indicate discs with and without structures, respectively. The best fit from MCMC linear regression is shown as a black solid line. 1000 random posterior fits are plotted using grey lines to visualize the fit uncertainty. We overplot a line corresponding to an optical depth of $\tau = \infty$ (dashed magenta line), assuming a dust temperature of 20 K.

Table 3. Summary of the fits.

Sample	x	y	α	β	σ	$\hat{\rho}$, CI$_\rho$
Total	$\log(F_{340\mathrm{GHz}})$/mJy	$\log(R_{90})$/au	$0.44^{+0.09}_{-0.10}$	$0.72^{+0.08}_{-0.07}$	$0.10^{+0.03}_{-0.02}$	0.87, (0.84, 0.89)
	$\log(F_{340\mathrm{GHz}})$/mJy	$\log(R_{68})$/au	$0.36^{+0.07}_{-0.06}$	$0.68^{+0.07}_{-0.06}$	$0.10^{+0.03}_{-0.02}$	0.86, (0.82, 0.88)
	$\log(M_\star)/\mathrm{M}_\odot$	$\log(F_{340\mathrm{GHz}})$/mJy	$1.71^{+0.15}_{-0.15}$	$1.83^{+0.22}_{-0.22}$	$0.21^{+0.05}_{-0.04}$	0.78, (0.72, 0.83)
	$\log(M_\star)/\mathrm{M}_\odot$	$\log(M_{\mathrm{dust}})/M_\oplus$	$1.14^{+0.15}_{-0.15}$	$1.83^{+0.22}_{-0.22}$	$0.21^{+0.05}_{-0.04}$	0.78, (0.72, 0.83)
	$\log(M_\star)/\mathrm{M}_\odot$	$\log(R_{90})$/au	$1.91^{+0.14}_{-0.13}$	$1.69^{+0.28}_{-0.24}$	$0.16^{+0.08}_{-0.05}$	0.81, (0.74, 0.87)
Structured	$\log(F_{340\mathrm{GHz}})$/mJy	$\log(R_{90})$/au	$1.13^{+0.10}_{-0.11}$	$0.36^{+0.07}_{-0.07}$	$0.04^{+0.02}_{-0.01}$	0.78, (0.67, 0.86)
	$\log(F_{340\mathrm{GHz}})$/mJy	$\log(R_{68})$/au	$1.00^{+0.10}_{-0.11}$	$0.38^{+0.07}_{-0.07}$	$0.05^{+0.02}_{-0.01}$	0.76, (0.65, 0.85)
Smooth and	$\log(F_{340\mathrm{GHz}})$/mJy	$\log(R_{90})$/au	$0.21^{+0.13}_{-0.15}$	$0.82^{+0.13}_{-0.11}$	$0.13^{+0.06}_{-0.04}$	0.83, (0.78, 0.87)
unresolved	$\log(F_{340\mathrm{GHz}})$/mJy	$\log(R_{68})$/au	$0.21^{+0.10}_{-0.14}$	$0.71^{+0.11}_{-0.09}$	$0.10^{+0.04}_{-0.03}$	0.82, (0.77, 0.87)
Only M3-K6	$\log(F_{340\mathrm{GHz}})$/mJy	$\log(R_{90})$/au	$0.40^{+0.16}_{-0.18}$	$0.81^{+0.14}_{-0.12}$	$0.12^{+0.05}_{-0.03}$	0.87, (0.81, 0.90)
	$\log(F_{340\mathrm{GHz}})$/mJy	$\log(R_{68})$/au	$0.27^{+0.15}_{-0.18}$	$0.79^{+0.14}_{-0.12}$	$0.10^{+0.04}_{-0.03}$	0.88, (0.83, 0.91)

Note. Summary of the fits of this study using LINMIX, assuming $y = \alpha + \beta x$. Upper limits are included when unresolved discs are part of the sample. The reported values correspond to the median, and the uncertainties represent the 68 per cent confidence interval. The variance σ or regression intrinsic scatter as well as the correlation coefficient (ρ) are reported with 68 per cent of their confidence intervals.

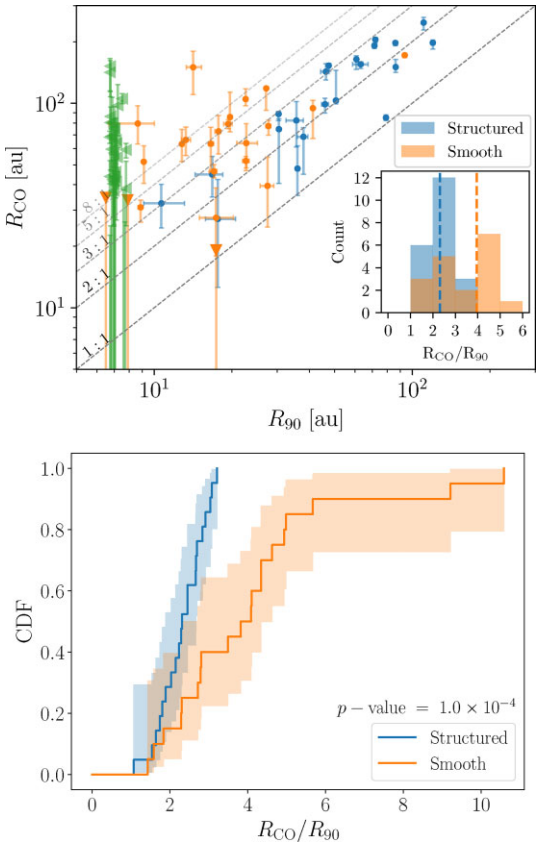

Figure 7. Top panel: R_{CO} versus R_{90} radius from dust continuum emission. The dashed lines indicate CO-to-continuum radius ratios equal to 1, 2, 3, 5, 8. The inset panel shows the histogram of the CO-to-continuum radius ratio for structured (blue) and smooth (orange) discs. Bottom panel: CDFs of the R_{CO}/R_{90} for the structured versus smooth discs in the UpperSco sample of this study.

not particularly different from the rest of the discs in terms of CO flux. Of the 10 that discs have values $R_{CO}/R_{90} > 4$, all of them are classified as smooth in our sample, which is consistent with radial drift of dust particles taking place and making the dust disc much smaller than the gaseous disc (L. Trapman et al. 2019; N. T. Kurtovic et al. 2021). None the less, the interpretation of R_{CO}/R_{90} in dust evolution models with and without pressure traps is complex, as it is shown in Section 4.5.

F. Long et al. (2022) analysed R_{CO}/R_{90} of a sample of 44 discs in several nearby star-forming regions, mostly Taurus, Lupus, and Ophiucus and found an averaged value of $R_{CO}/R_{90} = 2.9 \pm 1.2$. We compare the CDFs of the sample in F. Long et al. (2022) and our sources, and we did not find a significant variation of the distribution of the R_{CO}/R_{90} ratio between younger star forming regions and the value we find in UpperSco. In addition, F. Long et al. (2022) did not find a significant difference of R_{CO}/R_{90} between discs with structures and smooth discs. Similarly, in L. Trapman et al. (2025b) there are no significant difference in R_{CO}/R_{90} between Lupus and UpperSco, and no difference between structured and smooth discs. The difference of R_{CO}/R_{90} between smooth and structured discs is significant in our results, contrary to F. Long et al. (2022) and L. Trapman et al. (2025b).

We look at the distribution of R_{90}, and R_{CO}/R_{90} for the structured and smooth discs based on the spectral type of the central star (Fig. 8, top panels). There is a small trend of R_{90} decreasing for late type stars in both groups (structured and smooth discs), which leads to a modest trend of R_{CO}/R_{90} increasing for late type stars. In addition, we perform a similar analysis of the distribution of discs per the sub-clusters in UpperScorpius OB Association (described in S. Ratzenböck et al. 2023a), to check if the distribution of dust disc sizes changes across clusters, and therefore different ages between ∼4 and ∼14 Myr. We do not find any trend for R_{90} with age, but for R_{CO}/R_{90} there is a slight decrease for the smooth discs, while R_{CO}/R_{90} is approximately constant for structured discs, as shown in the bottom panels of Fig. 8.

Finally, we look for potential correlations of R_{90} and R_{CO}/R_{90}, as well as the millimetre fluxes, with environmental UV flux (G_0). The F_{UV} values are evaluated as the sum of the contribution of the surrounding OBA-type stars, where we accounted for the uncertainty in the separation between disc and massive stars in a 3D space. Specifically, given the 2D geometry of the stellar cluster, the local density function of the region can be defined, and therefore the probability distribution of the 3D separation from massive stars. We sampled from this probability to compute the distribution of the FUV flux (R. Anania et al. 2025b). We do not find any potential correlation of these quantities with F_{UV} (Fig. 9) in agreement with the results from Zagaria et al. (in preparation) for R_{CO}.

4.4 Disc dust mass versus stellar mass relationship

We derived the stellar mass for all possible targets in this work. For this, the effective temperatures are obtained from spectral types from C. F. Manara et al. (2020) if available, otherwise from K. L. Luhman (2022) using the conversions of M. J. Pecaut & E. E. Mamajek (2013). After correcting for extinction (using the extinction law from J. A. Cardelli, G. C. Clayton & J. S. Mathis 1989, and 2MASS and DENIS photometry), stellar luminosities are derived by scaling the 2MASS J observed photometries to the Gaia DR3 distances (using the geometric distances of C. A. L. Bailer-Jones et al. 2021). To derive stellar masses, the stellar luminosities and effective temperatures are then compared to an interpolated grid of I. Baraffe et al. (2015) pre-main sequence evolutionary tracks. A conservative 10 per cent error in stellar luminosity and effective temperature is applied to all sources. For 94 of the 285 sources of the whole sample in J. M. Carpenter et al. (2025), no luminosity could be obtained and hence no stellar mass is estimated because either there is a lack of data to compute effective temperatures or stellar luminosities, or because they fall outside pre-main sequence tracks in the HR diagram (the latter is only the case for two sources).

In terms of number of discs for which we can calculate stellar masses and for which we perform visibility analysis, we have the following: 18 of the 24 structured discs, 20 of the 28 smooth discs, and 54 of the 69 unresolved discs, for a total overlap of 92 discs in our sample. Fig. 10 shows the correlation between the flux at 340 GHz (left y-axis) or M_{dust} (right y-axis) versus the stellar mass. For the disc mass, we assume optically thin emission (R. H. Hildebrand 1983), that is:

$$M_{dust} = \frac{d^2 F_\nu}{\kappa_\nu B_\nu(T)}. \quad (8)$$

For κ_ν, we assume $\kappa_\nu = 2.3\ cm^2\ g^{-1} (\nu/230\,GHz)^{0.4}$ (e.g. S. M. Andrews et al. 2013), and B_ν is the blackbody surface brightness assuming a disc temperature of 20 K.

Previous works reported the M_{dust}–$M_\star$ for several star forming regions (e.g. S. M. Andrews et al. 2013; I. Pascucci et al. 2016; M. Ansdell et al. 2017), finding that this correlation is similar to

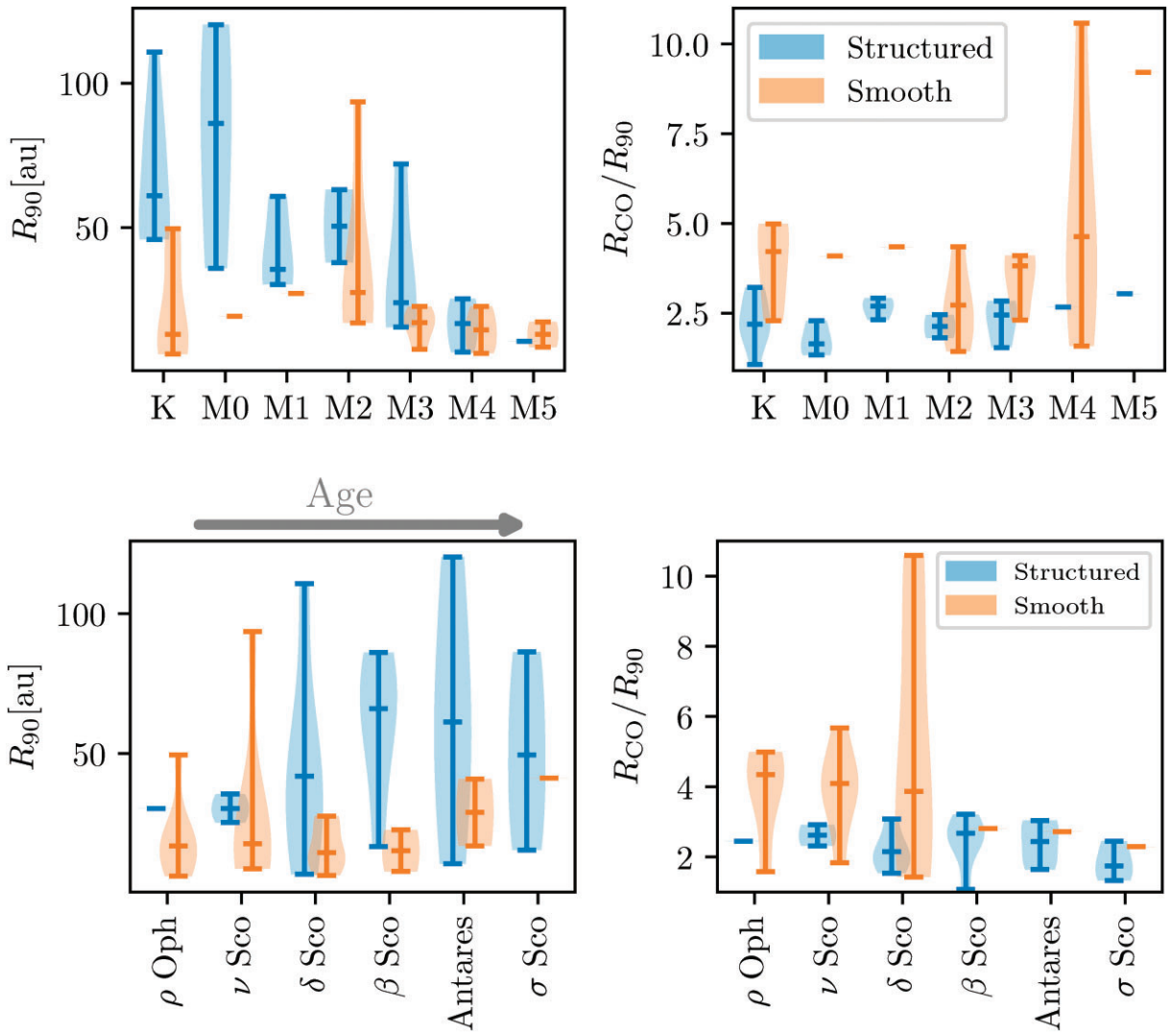

Figure 8. Distribution of R_{90}, R_{CO}, and R_{CO}/R_{90} for the structured (blue) and smooth (orange) discs based on the spectral type of the central star (top panels), and sub-region that they belong, organized by age (bottom panels). Some entries do not have a distribution because there are few number of discs in that bin.

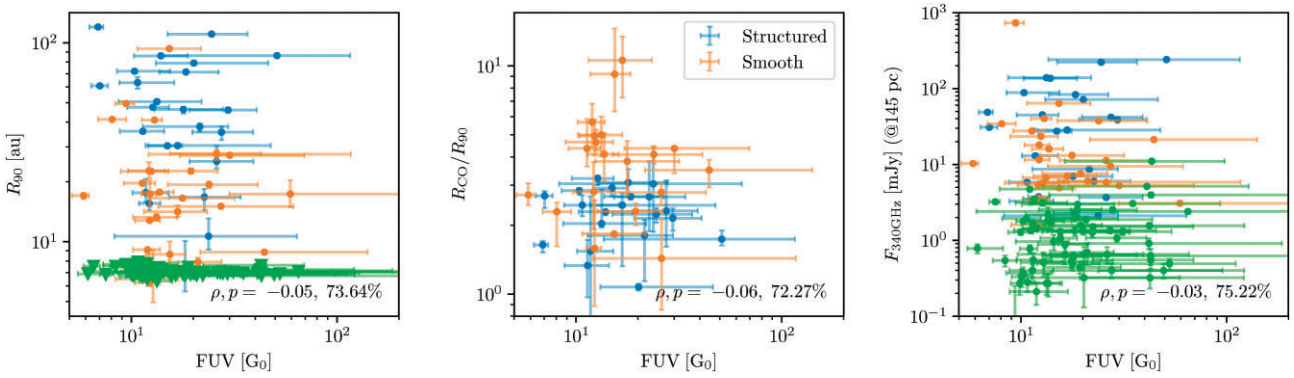

Figure 9. Disc properties against F_{UV}. Left: Dust continuum radius. Middle: Gas to dust size ratio. Right: Dust continuum flux at Band 7. Blue, orange, and green points represent structured discs, smooth discs, and unresolved discs, respectively.

the young star-forming regions of Taurus, Lupus, and Chamaeleon I ($M_{dust} \propto M_{\star}^{\sim 1.2-1.6}$), that are ∼1–3 Myr, but that steepens for the older star-forming region UpperSco ($M_{dust} \propto M_{\star}^{\sim 2.4-2.7}$). We fit the M_{dust}–$M_{\star}$ correlation using our data and including the unresolved discs, and the results are summarized in Table 3. Our best-fitting correlations is less steep than reported previously for UpperSco (S. A. Barenfeld et al. 2016; I. Pascucci et al. 2016), and similar to the values found in younger regions.

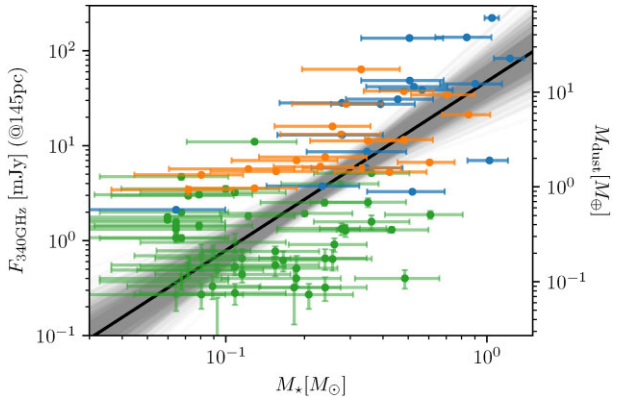

Figure 10. Flux (left *y*-axis) or M_{dust} (right *y*-axis) versus the stellar mass. The fluxes are normalized to a distance of 145 pc. Blue, orange, and black points represent the structured, smooth discs, and unresolved discs, respectively.

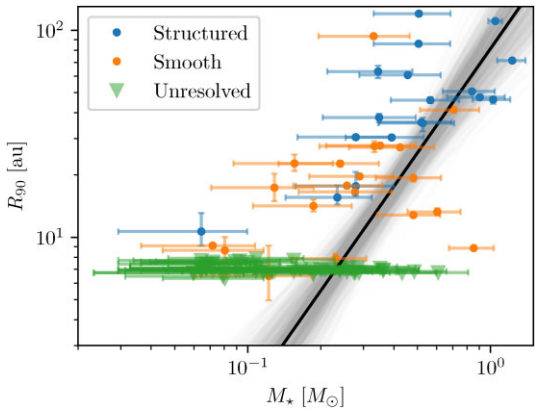

Figure 11. Dust disc size R_{90} versus stellar mass. Blue, orange, and black points represent the structured, smooth discs, and unresolved discs, respectively.

As the dust continuum flux is known to scale with stellar mass (in this work as $F_{340\,\mathrm{GHz}} \propto M_\star^{1.83}$), and the disc millimetre flux scales with dust disc radius (in this work as $R_{90} \propto F_{340\,\mathrm{GHz}}^{0.72}$, Section 4.2), it is expected that there is a correlation with $M_\star$ and R_{90}. Fig. 11 shows the correlation between the dust disc size R_{90} and stellar mass ($R_{90} \propto M_\star^{1.69}$), and the results of the fit are in Table 3. From the previous relations, one expects $R_{90} \propto M_*^{1.83*0.72}$, which is consistent within the uncertainties with the slope reported in Table 3. This correlation is strong and with very low chance to be random, as suggested by the ρ values. This correlation was not found in most of the star forming regions analysed by N. Hendler et al. (2020), but reported in S. M. Andrews et al. (2018) for Lupus and Taurus using Band 7 ALMA observations, with a much flatter slope of ∼0.6. As explained in S. M. Andrews et al. (2018), depending on if the dust emission is optically thick or thin, the expected correlation between $M_\star$ and R_{90} can be recovered with different slopes, although it is not straightforward in the case of optically thin emission as it would depend on the scaling relations of the disc temperature, dust surface density and optical depth. As the slope is higher in UpperSco compared to the values reported for younger discs in Lupus and Taurus, we suggest that this is because discs in UpperSco are less optically thick. Finally, we do not identify a clear difference between smooth and structured discs in these correlations of M_{dust}–$M_\star$ or R_{90}–$M_\star$.

4.5 Gas and dust evolution models

Fig. 12 shows an example of the dust density distribution as a function of grain size and distance from the star from the dust evolution simulations with $F_{\mathrm{UV}} = 10\,G_0$. These are shown for discs that are considered smooth (no traps) and discs with structures (weak, strong, and transition disc-type traps). The models shown in Fig. 12 correspond to discs around a 0.3 $\mathrm{M}_\odot$ stellar mass. The results for 1.0 $\mathrm{M}_\odot$ are shown in Fig. B2. All the models are shown at the same time of evolution, which is 2 Myr, which means 1 Myr after external photoevaporation has been active. This figure shows the effect of dust trapping for a given $G_0 = 10$, where traps help to accumulate dust in pressure maxima, keeping dust particles in the outer disc.

To investigate the potential effect of F_{UV} in the models, we investigate in Fig. 13 (for the case of discs around 0.3 $\mathrm{M}_\odot$) and 14 (for the case of discs around 1.0 $\mathrm{M}_\odot$) the evolution of the gas and dust disc mass directly obtained from the models, and the evolution of the gas and dust disc size as the location that encloses 90 per cent of the total gas and dust mass in the models. For the dust disc sizes, we assume the contribution of all the grain sizes in the simulations. In some cases, in the models of discs around a 0.3 $\mathrm{M}_\odot$ star, the disc disperses before the end of the simulation. We assume disc dispersion time when the disc gas mass is lower than 1 per cent of the initial gas disc mass. The time-step when this occurs is marked as a point in the figures. In the case of discs around a 0.3 $\mathrm{M}_\odot$ star, discs in 9/16 simulations dispersed before 5 Myr, while in the case of discs around a 1.0 $\mathrm{M}_\odot$ star, all discs still exist by the last time step of the simulations (10 Myr), in which case we also mark this last time step as point in the figures.

Fig. 13 shows that once external photoevaporation is active, the disc gas mass and size decreases sharper with time for models of discs around a 0.3 $\mathrm{M}_\odot$ star than in discs around a 1 $\mathrm{M}_\odot$ star (Fig. 14). This is a natural consequence of external photoevaporation as disc material is less gravitationally bound around a lower mass star, which makes it easier to disperse the disc by photoevaporation from the UV irradiation in the environment. Interestingly, for the models of discs around a 0.3 $\mathrm{M}_\odot$ star, there is a large difference of M_{gas} between $F_{\mathrm{UV}} = 1\,G_0$ and the rest of the F_{UV} values ($F_{\mathrm{UV}} = 10, 20, 40\,G_0$). But results do not change significantly among the models where F_{UV} is higher than 1 G_0, and already for $F_{\mathrm{UV}} = 10\,G_0$ the disc disperses by the ages of UpperSco. The dispersal time changes among models with different type of traps. However, this is a consequence of the method used to impose the traps in the disc evolution, which is by varying locally the α-viscosity. This impacts the gas accretion rate and hence the disc lifetime. In addition, as the time steps saved in the simulations are largely separated, it is difficult to recover the exact dispersion time, and therefore the difference in dispersion time-scales among models assuming different pressure traps should be taken with caution.

The evolution of the gas disc size also shows a fast decrease once the disc is truncated by the external photoevaporation. The truncation radius corresponds to the location where the wind transitions from optically thin to optically thick at UV wavelengths. In the simulations of discs around a 0.3 $\mathrm{M}_\odot$ star, this truncation happens right after external photoevaporation is active, which means right after 1 Myr of evolution, independent of the type of the value of G_0 and the type of pressure traps. R. Anania et al. (2025a) demonstrated that with these low values of G_0 the time-scale when disc truncation happens is not

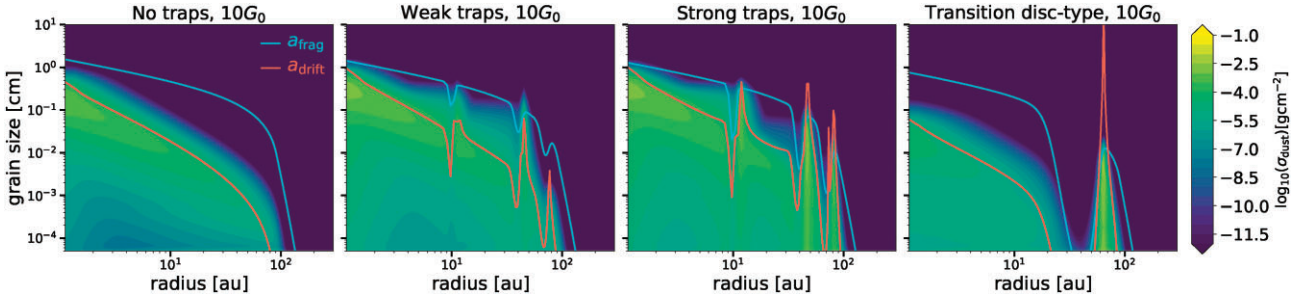

Figure 12. Dust density distribution after 2 Myr of evolution for discs with (from left to right): no traps, weak traps, strong-traps, and transition disc-type trap. All of these models assume a $F_{UV} = 10\,G_0$. These models are for the case of discs around a 0.3 $M_\odot$ star.

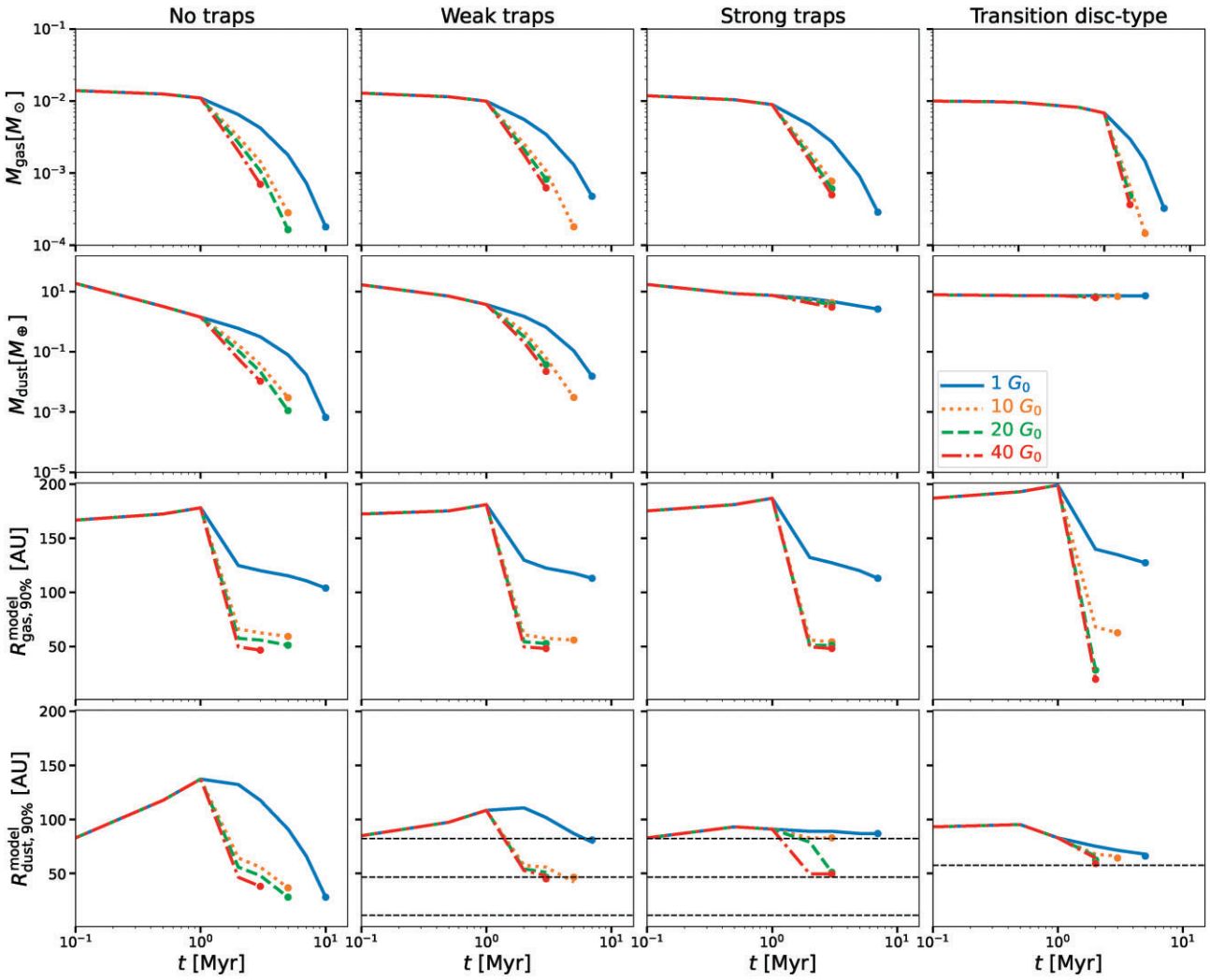

Figure 13. From top to bottom: evolution of the gas disc mass, dust disc mass, gas disc size, and dust disc size directly obtained from models with different values of F_{UV}. From left to right: no traps, weak traps, strong-traps, and transition-disc type trap. These are the results for the cases of a disc around a 0.3 $M_\odot$. The dots represent the last time step before the disc dissipates. Horizontal dashed lines are the location of the pressure maxima in the models with dust traps.

influenced by when external photoevaporation starts to influence the disc evolution. For testing this, R. Anania et al. (2025a) performed simulations in which the external F_{UV} is turned-on after 1 Myr (as in our models) and in this case the gas radius rapidly evolves to the same value when the disc experiences the same external radiation from earlier times of evolution, thus the same values are obtained over million-year time scales.

Comparing the evolution of the gas mass with the case of discs around a 1.0 $M_\odot$ star, we see that the effect of including photoevaporation is much weaker when $M_\star = 1.0\,M_\odot$ independent of the G_0 value. For the disc size evolution, there is a less noticeable influence of external photoevaporation, where only in the case of $F_{UV} = 40\,G_0$ the gas disc size decreases slowly with time after 1 Myr. For the other F_{UV} values, the gas disc either continues expanding or the gas size

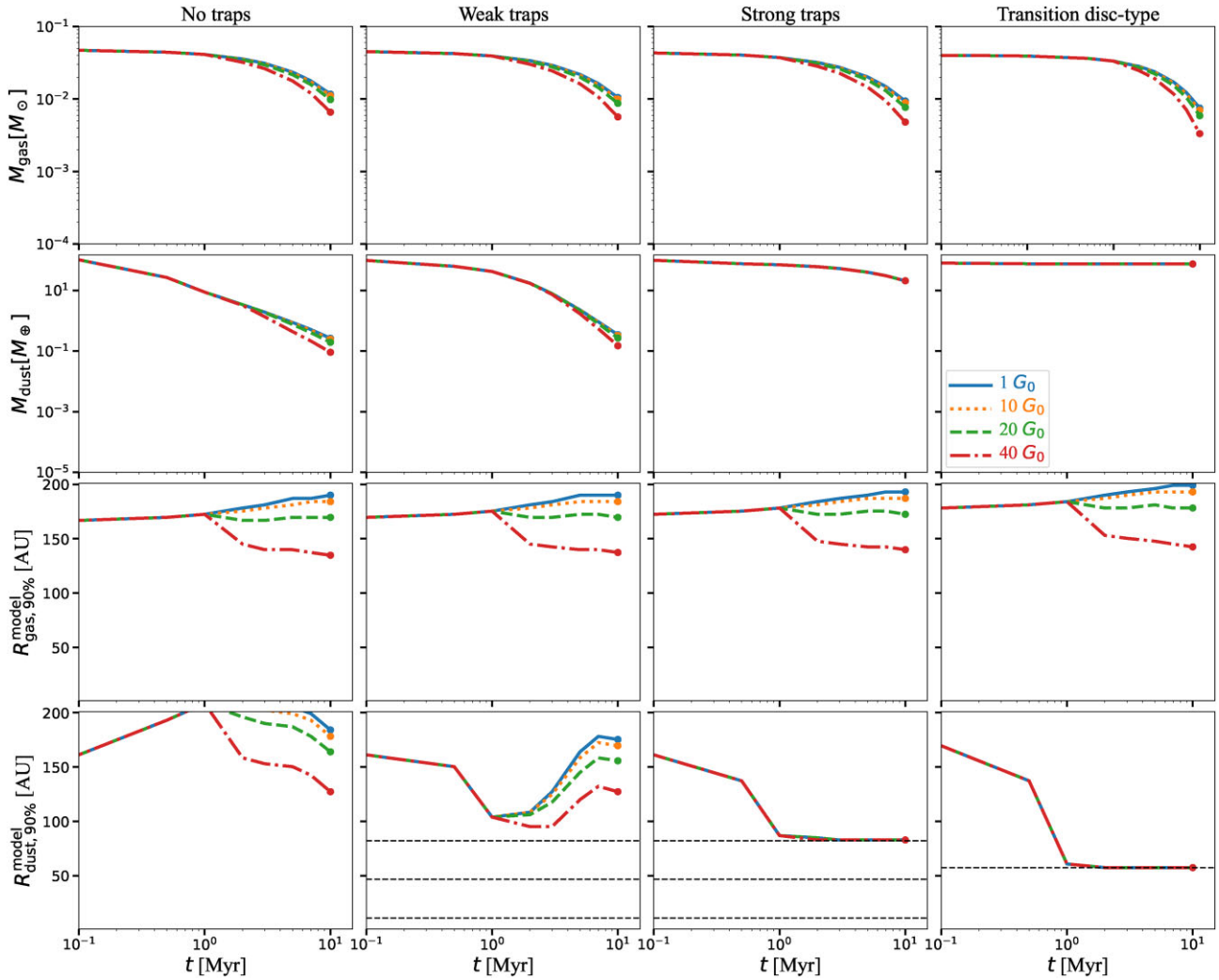

Figure 14. Same as Fig. 13 but for a 1 $M_\odot$ star.

remains approximately the same until the end of the simulations. This difference in the evolution of the gas disc size between 1.0 and 0.3 $M_\odot$ is mainly due to less gravitationally bound material around $M_\star = 0.3\,M_\odot$. The cut-off radius in both simulations is assumed the same, but as shown by M. Gárate et al. (2024) and R. Anania et al. (2025a), it does not have a strong effect in the gas evolution.

For the evolution of the dust mass and size, dust mass is more depleted in the cases of $M_\star = 0.3\,M_\odot$ than for $M_\star = 1.0\,M_\odot$. This is because radial drift is more efficient around lower mass stars (fig. 2 in N. der Marel & P. Pinilla 2023). Comparing Figs 13 and 14, it is possible to see how weak and strong traps ($A = 1, 4$) are more inefficient in retaining dust in discs around $M_\star = 0.3\,M_\odot$ (see also P. Pinilla et al. 2020). For the dust disc size, we see the effect of grain growth in the evolution, which makes the dust disc size to increase up to around 1 Myr, and in the absence of traps to quickly shrink with time once grains have reached sizes that effectively drift. This decrease of the disc size is less sharp with time when the pressure bumps are of higher amplitude, retaining dust more efficiently. In the case of $M_\star = 0.3\,M_\odot$, the dust disc size (directly obtained in the models assuming all grains sizes) continues to decrease in all the different types of traps that are assumed, converging to the location of one of the pressure maxima, depending on the values of F_{UV}. For $F_{UV} = 1, 10\,G_0$ the dust disc size converges to the location of the furthest pressure bump, while for higher F_{UV}, it converges to the middle pressure bump. This is discussed in more details in Section 4.6.

Contrary, in the case of $M_\star = 1.0\,M_\odot$, the dust disc size decreases in the presence of weak traps, but increases again with time. This is because we are assuming all grain sizes from the models in the calculation of the dust disc size, and the micron-sized particles contribute more to the total disc mass over time in the outer regions, creating an apparent increase of the dust disc size. For strong and transition-disc type traps, the dust disc size converges to nearly the location of the outer trap (or in the case of the transition disc, to the only pressure maxima present in the disc). In general, there is a low influence of G_0 for the evolution of the dust disc size and mass for the $M_\star = 1.0\,M_\odot$ case.

4.6 Synthetic observable disc properties

Fig. 15 show the evolution of the millimetre flux at 340 GHz, R_{90}, R_{CO} and R_{CO}/R_{90} for different values of G_0, which were calculated as described in Section 3.2. This figure shows the cases of discs around a 0.3 $M_\odot$ star with no traps, weak traps, strong-traps, and transition-disc type trap. The millimetre flux at 340 GHz, R_{90}, R_{CO} evolve similar to the dust disc mass (M_{dust}), the dust disc size from

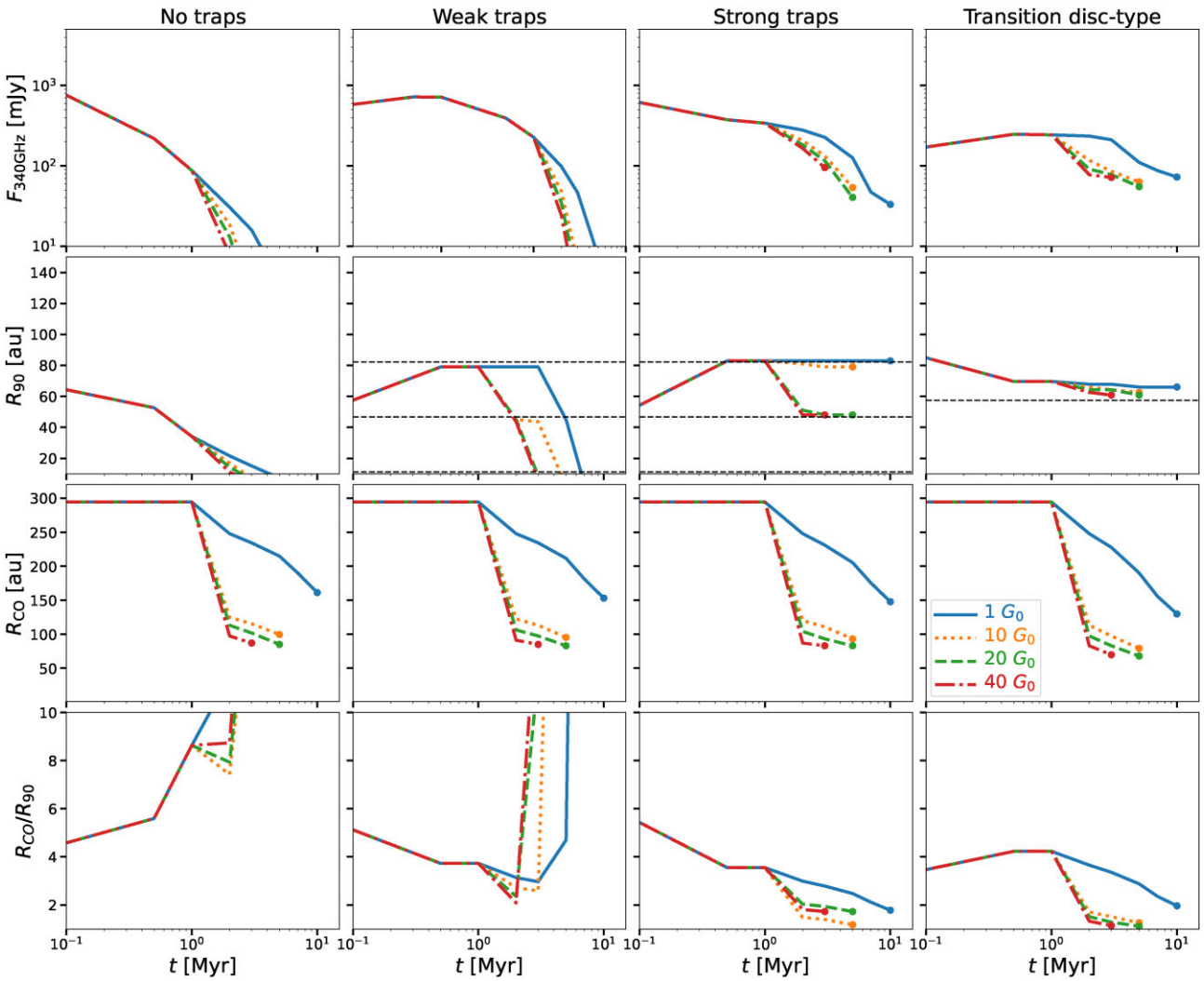

Figure 15. From top to bottom: evolution of the millimetre flux, R_{90}, R_{CO}, and R_{CO}/R_{90} for different values of F_{UV}. From left to right: no traps, weak traps, strong-traps, and transition-disc type trap. Horizontal dashed lines are the location of the pressure maxima in the models with dust traps. These results correspond to the models of discs around a 0.3 $M_\odot$ star.

the models ($R^{model}_{dust,90\ per\ cent}$), and the gas disc size from the models ($R^{model}_{gas,90\ per\ cent}$), respectively (Fig. 13 and 14).

For $M_\star = 0.3\,M_\odot$, the millimetre continuum fluxes sharply decrease over time in the absence of traps or with weak traps, while with strong traps or transition-disc traps there is less decrease over time because particles are efficiently trapped over million-year timescales, which helps to maintain detectable levels of millimetre flux. The value of R_{90} initially increases with time (within the first 1 Myr) when millimetre-sized particles are growing in the outer disc, but once drift becomes efficient (>1 Myr), R_{90} decreases with time in the case of no traps or weak traps. In the case of strong traps, for the cases of $F_{UV} = 1, 10\,G_0$, R_{90} converges to the location of the furthest pressure bump, which is around 82 au. However, for $F_{UV} = 20, 40\,G_0$, R_{90} converges to the location of the second pressure bump around 47 au. This is because the further out pressure bump is outside the truncation radius, which is around 50 au in these cases (Fig. 13). M. Gárate et al. (2024) showed that when a trap with a similar amplitude than assumed for the strong traps ($A = 4$) is outside the truncation radius, it quickly dispersed for much higher values of G_0 than what we assume in this work. Hence, we now demonstrate that already for $G_0 \geq 20$, pressure bumps with an amplitude of $A = 4$ outside the truncation radius are inefficient on trapping dust particles for discs around a 0.3 $M_\odot$ star. Interestingly, for the case of a transition disc-type trap, which is of very high amplitude, the R_{90} converges to the location of the only pressure trap, which is around 58 au for all the values of F_{UV}. This implies that such strong pressure makes R_{90} to trace the location of the dust trap before the disc disperses, independent of the F_{UV} value assumed for the discs in UpperSco.

The ratio of the gas to dust disc size R_{CO}/R_{90} shows very different evolution that strongly depends on the type of traps, but only slightly depends on the values of F_{UV}. For no traps or weak traps, R_{CO}/R_{90} initially has values of around 4, and it continues increasing over time, which is a result of efficient drift, and it agrees with previous results (e.g. L. Trapman et al. 2019; C. Toci et al. 2021). For strong traps or transition disc-type traps, the R_{CO}/R_{90} starts with similar values of 4, but starts to decrease once millimetre-sized particles have grown and drift towards pressure maxima, while the gas disc size keeps decreasing due to the truncation by external photoevaporation. The combination of these two effects, makes R_{CO}/R_{90} to reach

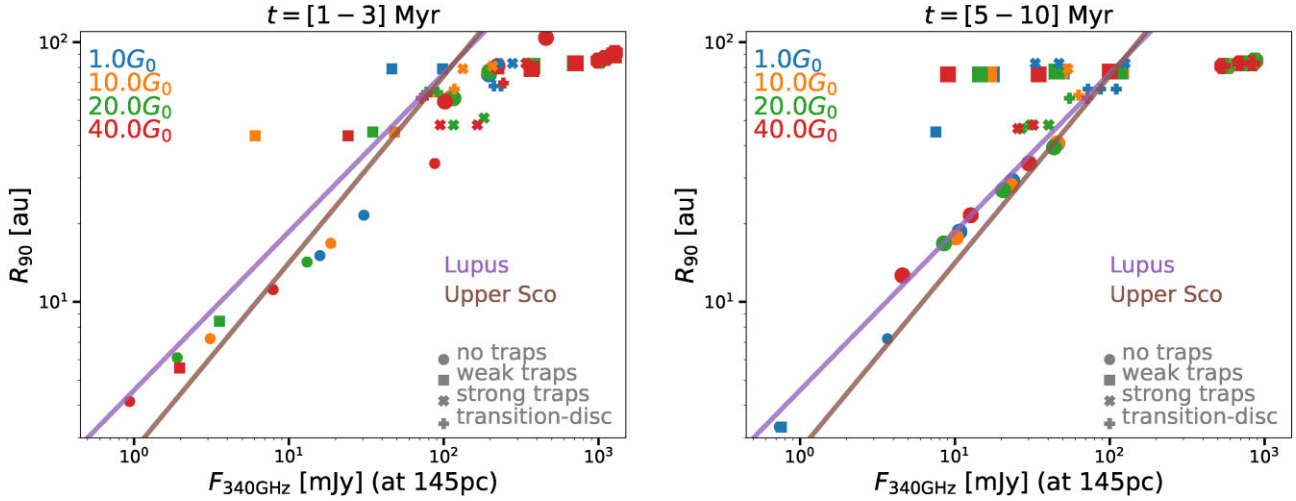

Figure 16. Disc millimetre luminosity versus dust disc radius R_{90} from the models for different values of $F_{\rm UV}$ and traps, assuming the outputs from 1–3 Myr (left panel) or 5–10 Myr (right panel). The colours represent different values of $F_{\rm UV}$, while the shape of the points the type of pressure traps. The size of the points symbolize different stellar masses (small size for $M_\star = 0.3\,{\rm M}_\odot$ and larger sizes for $M_\star = 1.0\,{\rm M}_\odot$). As a reference, the best observational fit found for Lupus (O. M. Guerra-Alvarado et al. 2025) and UpperSco (this work) is overplotted.

values as low as ∼1.2 before the disc disperses. The exact value of $R_{\rm CO}/R_{90}$ would depend on where pressure bumps are assumed, so the trends when considering different traps and different $F_{\rm UV}$ over million-year times of evolution is the key when comparing with observations of discs in different evolutionary stage (rather than the values themselves).

Fig. B3 in the Appendix B shows the evolution of the millimetre flux at 340 GHz, R_{90}, $R_{\rm CO}$, and $R_{\rm CO}/R_{90}$ for the case of $M_\star = 1\,{\rm M}_\odot$. The main differences with the case of $M_\star = 0.3\,{\rm M}_\odot$ is that because photoevaporation and drift are less effective, $R_{\rm CO}$ decreases less with time and R_{90} converges to the location of the further dust trap independent of the amplitude of the bumps assumed. As a consequence, while $R_{\rm CO}/R_{90}$ sharply increases over time for no traps, $R_{\rm CO}/R_{90}$ slightly increases for the other trap cases, reaching values between $3-5$ and remaining almost constant between 1–10 Myr.

Fig. 16 shows the disc millimetre luminosity versus dust disc radius R_{90} from the models for different values of $F_{\rm UV}$, traps, $M_\star$, and different times of evolution. The main results of this figure are: (1) The values of $F_{\rm UV}$ do not have a strong influence on the potential correlation, as the different values (shown by different colours) are distributed everywhere in the plot, meaning that they do not drive any potential correlation in the models. (2) The presence or absence of traps has the highest impact on a potential correlation. Models with no traps or weak traps have lower millimetre fluxes and lower R_{90}, resembling a correlation similar to the observed ones in Lupus and UpperSco, while models with stronger traps remain with higher fluxes and dust disc sizes, potentially explaining discs located in the upper right part of the dust disc size–luminosity relationship (Fig. 6). The low mass stars drive the correlation at earlier times (1–3 Myr), while the Solar-mass stars drive the correlation at later times (5–10 Myr) as at this late stages the disc has dispersed in several of the models with $M_\star = 0.3\,{\rm M}_\odot$ as explained above. It is important to note that although in this work we focus on investigating the effect of different values for external photoevaporation and pressure bumps, different other parameters, such as disc viscosity and fragmentation velocity can highly influence this correlation as shown in A. Zormpas et al. (2022).

5 DISCUSSION

5.1 Dust disc size, gas-to-dust disc ratio and their evolution

The age of the UpperSco star forming region is typically considered to be between 3 and 10 Myr old (or even older, e.g. M. J. Pecaut et al. 2012; K. L. Luhman & T. L. Esplin 2020; J. J. Armstrong et al. 2025), which corresponds to the late stages of disc evolution (e.g. D. Fedele et al. 2010). The comparison of different disc properties with younger star forming regions, such as Lupus and Taurus allow testing evolutionary effects. However, in contrast to other nearby young star forming regions, the discs in UpperSco are exposed to moderate values of $F_{\rm UV}$ radiation from the OBA-type stars in the association, which challenges the comparison with younger star forming regions. For this reason, it is key to compare with gas and dust evolution models that include external photoevaporation to better understand what physical mechanisms dominate the evolution and shape the observed properties.

The analysis of the morphology of the dust continuum emission of the discs resolved in UpperSco shows that discs with structures are significantly larger than smooth discs. O. M. Guerra-Alvarado et al. (2025) reached the same conclusion when analysing a sample of discs in Lupus, which age is ∼1–3 Myr old. In addition, there is no significant difference of the CDFs of the dust disc size of the UpperSco sample when comparing with the Lupus sample from O. M. Guerra-Alvarado et al. (2025), suggesting no evolution of the dust disc size from the intermediate ages of discs (∼1–3 Myr) to the later stages in UpperSco ($\gtrsim$3–10 Myr). This conclusion extends when the samples are split between structured and smooth discs (Fig. 5).

A more homogenous analysis of the disc dust and gas size throughout different star forming regions, including Lupus and UpperSco, was done in the AGE-PRO ALMA collaboration, which had a spatial resolution from 0.1–0.3 arcsec. From their analysis, they also found no significant variation of R_{90} between Lupus and UpperSco (M. Vioque et al. 2025; K. Zhang et al. 2025), in agreement with the results of this work. But since the uncertainties are large because in AGE-PRO there were only 10 stars in each star forming region, there was a wide range of outcomes still possible, and their results only place an upper limit on the changes. We confirm in this

study that there is no significant variation of R_{90} between Lupus and UpperSco.

In contrast, the millimetre continuum fluxes are known to be lower for UpperSco compared to younger star-forming regions (see for example fig. 2 in A. Miotello et al. 2023). Potential explanations of the decrease of the millimetre flux over time include dust radial drift (G. P. Rosotti et al. 2019; C. Toci et al. 2021; J. Stadler et al. 2022; L. Delussu et al. 2024), planetesimal formation (e.g. L. M. Bernabò et al. 2022), and the lost of dust particles by external factors (such as photoevaporation; A. D. Sellek et al. 2020). In the case of dust radial drift, it is possible that while the millimetre fluxes decrease over time, the dust disc radius remains nearly constant over time. This can happen in the presence of leaky dust traps, where the radial drift of the dust particles is reduced (not fully suppressed) since early stages (<1 Myr) of the disc evolution P. Pinilla et al. (2020) and N. T. Kurtovic et al. (2025). If these are leaky, the observed millimetre flux decreases over time, while the dust disc size traces the location of the furthest dust trap, as also proposed by M. Vioque et al. (2025) to explain the lack of evolution in the observed dust disc sizes of the AGE-PRO sample, while the millimetre fluxes decrease with age.

Our gas and dust evolution models demonstrate that these results of dust radial drift and trapping remain similar with the inclusion of mild external photoevaporation. However, this strongly depends on the mass of the hosting star, as a disc around a low mass star can be dispersed by external photoevaporation even with low values of $F_{\rm UV}$ irradiation ($F_{\rm UV}$ = 10–40 G_0). In these cases, the dust traps that are located outside the photoevaporative truncation radius are destroyed, preventing the traps to keep dust particles in the outer disc and reducing the dust disc radius over time, as well as the gas disc radius. However, M. Gárate et al. (2024) suggested that the dust particles entrained by the photoevaporative winds may shield the disc from external irradiation, decreasing the total mass loss rate. This potential shielding is not included in our models, and it will be a subject of research in the future.

We also investigated a potential variation of the dust disc size with the sub-regions where the discs are located (tracing different ages; S. Ratzenböck et al. 2023b; bottom panels in Fig. 8). We do not find a significant variation of the dust disc size within the sub-regions of the UpperSco association. This is in agreement with the models, where the discs that survive by the age of UpperSco are discs with structures, in which case no significant variation of the dust disc size is expected. However, we find a moderate decrease of $R_{\rm CO}/R_{90}$ for the smooth discs with the age of the region, contrary to model expectations; while $R_{\rm CO}/R_{90}$ remains approximately constant for structured discs as expected from models. This highlights the importance of deeper and higher angular resolution of the gas and dust of the discs classified as smooth in this work. As for example, low contrast small structures, such as the rings observed in TW Hya (S. M. Andrews et al. 2016; J. D. Ilee et al. 2022; S. Das, N. T. Kurtovic & M. Flock 2024), would not be resolved by the angular resolution and sensitivity of this work.

Our analysis also suggests that the millimetre fluxes, the dust disc size, and the gas-to-dust disc size ratio do not change with different values of the $F_{\rm UV}$ (Fig. 9). However, in clusters where the $F_{\rm UV}$ values are higher, such as Orion, σ Orionis and NGC 2024, previous works have shown that dust disc masses decline with decreasing separation from the photoionizing source, i.e. with higher $F_{\rm UV}$ (e.g. R. K. Mann et al. 2014, 2015; M. Ansdell et al. 2017; S. E. Terwisga et al. 2020; S. E. Terwisga & A. Hacar 2023).

In our gas/dust evolution models, the gas-to-dust disc size ratio is expected to increase with time in the absence of traps. This is also the case if the traps are weak (in our models when $A = 1$), and for the discs around a 0.3 $M_\odot$. Our observations suggest that the gas-to-dust disc size does not change significantly when comparing the values found in F. Long et al. (2022) primarily for discs in Lupus and Taurus versus the values that we found in UpperSco. The same conclusion was found in the AGE-PRO collaboration (L. Trapman et al. 2025b; K. Zhang et al. 2025). Therefore, the comparison of the models with observations suggest that traps need to be present in a significant fraction of the surviving discs. As a 0.3 $M_\odot$ is a more representative type of star in UpperSco, this would imply that these traps need to be strong by the age of UpperSco.

In our UpperSco sample, there are a couple of discs with extreme values of $R_{\rm CO}/R_{90}$ ($\gtrsim$6). Interestingly, two of them (2MASS-J16111705-2213085 and 2MASS-J16054540-2023088) are very low mass stars ($\sim$0.08 and $\sim$0.13 $M_\odot$, respectively). Our models predict that for these discs, $R_{\rm CO}/R_{90}$ would only reach those high values if no-traps or weak-traps are present (Fig. 15). However, they are not expected to survive more than 5 Myr with their $F_{\rm UV}$ values, which are for both between 16–17 G_0. A more detailed analysis of the potential initial conditions that can lead to the survival of these discs is subject in Ping et al. (in preparation).

Finally, in this work, we look for any correlation between the dust disc size (R_{90}) and the stellar properties. We found that the dust disc size is smaller for lower mass stars, while the gas disc size does not seem to change with stellar mass, as shown is Zagaria et al. (in preparation). As a consequence, the gas-to-dust disc size ratio seems to increase for low mass stars. This could be an effect of dust drift being more efficient around lower mass stars, making the dust disc size smaller in lower mass stars (P. Pinilla et al. 2013; P. Pinilla 2022). Interestedly, we find a correlation between R_{90} and $M_\star$, which is steeper than previously reported for discs in Taurus and Lupus (S. M. Andrews et al. 2018), which can be explained by less optical depth of the surviving discs in UpperSco.

5.2 Dust disc size versus luminosity

We find a strong relation between the disc luminosity and the dust disc size for the discs in UpperSco, which is steeper than reported in previous works for UpperSco (e.g. S. A. Barenfeld et al. 2016; N. Hendler et al. 2020). When compared the correlation with the recent work from O. M. Guerra-Alvarado et al. (2025) in Lupus, we find that this correlation is similar between Lupus and UpperSco, contrary to the results in N. Hendler et al. (2020).

This correlation has been analysed in different theoretical works, concluding that it can be explained by the drift of dust particles (e.g. G. P. Rosotti et al. 2019; A. Zormpas et al. 2022). In our models of gas/dust evolution that include external photoevaporation $F_{\rm UV}$ = 1, 10, 20, 40 G_0 and drift (that can also be reduced or stoped by pressure traps), we demonstrated that the effect of drift dominates the correlation and that there is no significant effect of $F_{\rm UV}$ for the discs that survive (Fig. 16). In late stages, the correlation is driven by the discs that survive mainly around a 1.0 $M_\odot$. Hence, $F_{\rm UV}$ does have an effect on what discs populate this relationship. It is therefore important to study the survival rate of discs in UpperSco in more detail by performing population synthesis models with a more dense parameter space of disc and stellar conditions (Ping et al., in preparation).

This correlation can be flattened by the presence of traps, as seen in Fig. 16 and shown in P. Pinilla et al. (2020). Our results show that the flattening of this relation is very effective in the presence of strong traps or transition disc-type traps (Fig. 16). This sharp transition between steep (for none traps) and flat (for strong traps) may be smoother when assuming traps that become stronger over

time and potential shielding due to dust particles in the wind that can help for the survival of discs around low mass stars. At the current resolution of our observations, we find a significant difference of the slope between structured versus smooth discs in the UpperSco sample, with the structured discs showing a flatter relation (Table 3), in agreement with model expectations.

6 CONCLUSIONS

In this work, we model the visibilities of the dust continuum emission of 121 discs in UpperSco from J. M. Carpenter et al. (2025), to constrain their flux, size, and geometry. Our visibility model assumes either a simple Gaussian profile with free centreing, or point sources for the unresolved and faint discs. We compare the observations with gas and dust evolution models that include external photoevaporation. Our main conclusions are:

(i) In our sample, 20 per cent of the discs are structured, 23 per cent remain smooth, and 57 per cent remain unresolved with the current resolution of the observations (0.1 arcsec–0.3 arcsec). The median value of R_{90} of the whole sample is $25.4^{+10.2}_{-7.7}$ au. When compared with the recent work of O. M. Guerra-Alvarado et al. (2025), there is no significant difference of the CDFs of Lupus and UpperSco, meaning that there is no a significant difference of R_{90} among the discs in Lupus and the surviving discs in UpperSco. In our analysis, there is a significant difference between the CDFs of the structured versus smooth discs in UpperSco, where the structured discs are significantly larger than the smooth discs (Table 2).

(ii) The dust disc size versus luminosity relationship in UpperSco is such that $R_{90} \propto L_{\rm mm}^{0.72}$, which is steeper than reported in previous works that analysed a smaller sample of UpperSco. This correlation is similar than in Lupus, where it is $R_{90} \propto L_{\rm mm}^{0.61}$, suggesting that this correlation does not change with disc evolution.

(iii) In our UpperSco sample, smooth discs have a significantly larger gas to dust disc size ratio ($R_{\rm CO}/R_{90}$) than structured discs. There is not a significant difference of $R_{\rm CO}/R_{90}$ when compared to the values found in younger discs (e.g. F. Long et al. 2022), in agreement with L. Trapman et al. (2025b). In addition, there is the modest trend of R_{90} decreasing for very low mass stars in both groups (structured and smooth discs). Such a trend is not seen in $R_{\rm CO}$ (Zagaria et al., in preparation), and hence a modest trend of $R_{\rm CO}/R_{90}$ increasing for low mass stars is driven by the changes of R_{90}.

(iv) There are no significant differences of R_{90} across the different sub-clusters that span ages between ∼4–14 Myr. $R_{\rm CO}/R_{90}$ seems to slightly decrease with age for the smooth discs, while it remains approximately constant for structured discs. Finally, no significant trends exist of R_{90} or $R_{\rm CO}/R_{90}$ versus the environmental UV flux.

(v) We find a dust disc mass versus stellar mass relationship, such that $M_{\rm dust} \propto M_\star^{1.83}$, which is flatter than previously reported for UpperSco, and it is similar to the correlation found in younger star-forming regions. We find a clear correlation between R_{90} versus stellar mass ($R_{90} \propto M_\star^{1.69}$), which is steeper than in Lupus and Taurus ($R_{90} \propto M_\star^{0.6}$; S. M. Andrews et al. 2018), suggesting that the surviving discs in UpperSco are less optically thick, which could be tested with future multiwavelengths observations.

(vi) The gas and dust evolution models that include mild values of $F_{\rm UV}$, show that discs around a low mass star (0.3 $M_\odot$) should have already dispersed by the age of UpperSco with the initial conditions assumed in this work. A population synthesis approach is needed to quantify the dispersion rate due to external photoevaporation with a larger parameter space exploration than in this work (Ping et al. in preparation). For dust disc size versus luminosity relationship, our models demonstrate that the values of $F_{\rm UV}$ do not have a strong influence on this correlation, and the presence or absence of traps (that controls the level of drift) has the highest impact on this correlation. In the models, the dust disc size versus luminosity relationship flattens when dust drift is reduced or suppressed in the presence of dust traps. This agrees with observations as this correlation for the structured discs is significantly flatter than for the smooth and unresolved discs.

(vii) The evolution of $R_{\rm CO}/R_{90}$ from the models is that it increases with age in the absence of pressure traps. For a 1 $M_\odot$ star, the presence of weak traps is enough to keep $R_{\rm CO}/R_{90}$ nearly constant over the last ten million years of the disc evolution. None the less, this is not the case for discs around a 0.3 $M_\odot$ star, for which only strong traps keep the $R_{\rm CO}/R_{90}$ value low and constant in the last million years of evolution. Comparing with observations, this suggests that for the surviving discs in UpperSco, most of the traps should be stronger than in earlier ages.

(viii) Higher resolution observations are needed to confirm several of the observed trends and values, specially to compare to surveys of younger regions that have been observed at higher resolution. It is surprising that despite models predicting that discs around 0.3 $M_\odot$ should have been dispersed by the age of 5 Myr, they still exist. This highlights the need of population synthesis models that include external photoevaporation in parallel to higher resolution observations, specially of the gas emission, to better understand the initial conditions, evolution and fate of these discs.

ACKNOWLEDGEMENTS

We are very thankful to Francesco Zagaria, Giovanni Rosotti, and Leon Trapman for providing the gas disc sizes used in this work prior to their publication, and for the scientific discussions. AS and PP acknowledge funding from the UK Research and Innovation (UKRI) under the UK government's Horizon Europe funding guarantee from ERC (under grant agreement no. 101076489). NK acknowledge funding from the Deutsche Forschungsgemeinschaft (DFG, German Research Foundation) – 325594231, FOR 2634/2. Support for FL was provided by NASA through the NASA Hubble Fellowship grant #HST-HF2-51512.001-A awarded by the Space Telescope Science Institute, which is operated by the Association of Universities for Research in Astronomy, Incorporated, under NASA contract NAS5-26555. RA acknowledges support from the European Union (ERC Starting Grant DiscEvol, project number 101039651) and from Fondazione Cariplo, grant no. 2022–1217. Views and opinions expressed are, however, those of the author(s) only and do not necessarily reflect those of the European Union or the European Research Council. Neither the European Union nor the granting authority can be held responsible for them.

This paper makes use of the following ALMA data: ADS/JAO.ALMA#2011.0.00526.S, ADS/JAO.ALMA#2013.1,00395.S, and ADS/JAO.ALMA#2018.1.00564.S. ALMA is a partnership of ESO (representing its member states), NSF (USA) and NINS (Japan), together with NRC (Canada), MOST and ASIAA (Taiwan), and KASI (Republic of Korea), in cooperation with the Republic of Chile. The Joint ALMA Observatory is operated by ESO, AUI/NRAO and NAOJ.

Software: This work made use of the following software: ASTROPY (Astropy Collaboration 2013, 2018), CASA (J. P. McMullin et al. 2007), DUSTPY (S. M. Stammler & T. Birnstiel 2022), EMCEE (D. Foreman-Mackey et al. 2013), GALARIO (M. Tazzari et al. 2018), MATPLOTLIB (J. D. Hunter 2007), NUMPY (C. R. Harris et al. 2020),

SCIPY (P. Virtanen et al. 2020), LINMIX (B. C. Kelly 2007), LIFELINES (C. Davidson-Pilon et al. 2019).

DATA AVAILABILITY

The data from observations and models underlying this article will be shared on request to the corresponding author. The non-calibrated ALMA data is publicly available at https://almascience.nrao.edu/aq/ using the project codes 2011.0.00526.S, 2013.1,00395.S, and 2018.1.00564.S. Complete tables of the stellar and disc properties obtained in this work are available in zenodo at https://doi.org/10.5281/zenodo.17182603

REFERENCES

Agurto-Gangas C. et al., 2025, ApJ, 989, 4
Anania R. et al., 2025a, ApJ, 989, 8
Anania R., Winter A. J., Rosotti G., Vioque M., Zari E., Pantaleoni González M., Testi L., 2025b, A&A, 695, A74
Andrews S. M., Rosenfeld K. A., Kraus A. L., Wilner D. J., 2013, ApJ, 771, 129
Andrews S. M. et al., 2016, ApJ, 820, L40
Andrews S. M., Terrell M., Tripathi A., Ansdell M., Williams J. P., Wilner D. J., 2018, ApJ, 865, 157
Ansdell M. et al., 2016, ApJ, 828, 46
Ansdell M., Williams J. P., Manara C. F., Miotello A., Facchini S., van der Marel N., Testi L., van Dishoeck E. F., 2017, AJ, 153, 240
Armstrong J. J., Tan J. C., Wright N. J., Jeffries R. D., Kos J., Fiorellino E., Buder S., Barrios Lopez D., 2025, MNRAS, preprint (arXiv:2505.03716)
Astropy Collaboration, 2013, A&A, 558, A33
Astropy Collaboration, 2018, AJ, 156, 123
Bae J., Isella A., Zhu Z., Martin R., Okuzumi S., Suriano S., 2023, in Inutsuka S., Aikawa Y., Muto T., Tomida K., Tamura M., eds, ASP Conf. Ser. Vol. 534, Protostars and Planets VII. Astron. Soc. Pac., San Francisco, p. 423
Bailer-Jones C. A. L., Rybizki J., Fouesneau M., Demleitner M., Andrae R., 2021, AJ, 161, 147
Baraffe I., Homeier D., Allard F., Chabrier G., 2015, A&A, 577, A42
Barenfeld S. A., Carpenter J. M., Ricci L., Isella A., 2016, ApJ, 827, 142
Bernabò L. M., Turrini D., Testi L., Marzari F., Polychroni D., 2022, ApJ, 927, L22
Cardelli J. A., Clayton G. C., Mathis J. S., 1989, ApJ, 345, 245
Carpenter J. M., Esplin T. L., Luhman K. L., Mamajek E. E., Andrews S. M., 2025, ApJ, 978, 117
Cieza L. A. et al., 2019, MNRAS, 482, 698
Das S., Kurtovic N. T., Flock M., 2024, A&A, 689, A104
Davidson-Pilon C. et al., 2019, CamDavidsonPilon/lifelines, Zenodo, Version v0.23.4
Delussu L., Birnstiel T., Miotello A., Pinilla P., Rosotti G., Andrews S. M., 2024, A&A, 688, A81
Dutrey A., Guilloteau S., Prato L., Simon M., Duvert G., Schuster K., Menard F., 1998, A&A, 338, L63
Facchini S., Birnstiel T., Bruderer S., van Dishoeck E. F., 2017, A&A, 605, A16
Fedele D., van den Ancker M. E., Henning T., Jayawardhana R., Oliveira J. M., 2010, A&A, 510, A72
Foreman-Mackey D., Hogg D. W., Lang D., Goodman J., 2013, PASP, 125, 306
Gárate M., Pinilla P., Haworth T. J., Facchini S., 2024, A&A, 681, A84
Guerra-Alvarado O. M., van der Marel N., Williams J. P., Pinilla P., Mulders G. D., Lambrechts M., Sanchez M., 2025, A&A, 696, A232
Guilloteau S., Dutrey A., 1998, A&A, 339, 467
Gundlach B., Blum J., 2015, ApJ, 798, 34
Harris C. R. et al., 2020, Nature, 585, 357
Haworth T. J., Clarke C. J., Rahman W., Winter A. J., Facchini S., 2018, MNRAS, 481, 452
Haworth T. J., Coleman G. A. L., Qiao L., Sellek A. D., Askari K., 2023, MNRAS, 526, 4315
Hendler N., Pascucci I., Pinilla P., Tazzari M., Carpenter J., Malhotra R., Testi L., 2020, ApJ, 895, 126
Hildebrand R. H., 1983, QJRAS, 24, 267
Hunter J. D., 2007, Comput. Sci. Eng., 9, 90
Ilee J. D., Walsh C., Jennings J., Booth R. A., Rosotti G. P., Teague R., Tsukagoshi T., Nomura H., 2022, MNRAS, 515, L23
Kelly B. C., 2007, ApJ, 665, 1489
Kenyon S. J., Hartmann L., 1987, ApJ, 323, 714
Kurtovic N. T. et al., 2021, A&A, 645, A139
Kurtovic N. T. et al., 2025, ApJ, 989, 6
Lissauer J. J., Batalha N. M., Borucki W. J., 2023, in Inutsuka S., Aikawa Y., Muto T., Tomida K., Tamura M., eds, ASP Conf. Ser. Vol. 534, Protostars and Planets VII. Astron. Soc. Pac., San Francisco, p. 839
Long F. et al., 2019, ApJ, 882, 49
Long F. et al., 2022, ApJ, 931, 6
Luhman K. L., 2022, AJ, 163, 24
Luhman K. L., Esplin T. L., 2020, AJ, 160, 44
Lynden-Bell D., Pringle J. E., 1974, MNRAS, 168, 603
Manara C. F. et al., 2020, A&A, 639, A58
Mann R. K. et al., 2014, ApJ, 784, 82
Mann R. K., Andrews S. M., Eisner J. A., Williams J. P., Meyer M. R., Di Francesco J., Carpenter J. M., Johnstone D., 2015, ApJ, 802, 77
Mathis J. S., Rumpl W., Nordsieck K. H., 1977, ApJ, 217, 425
McMullin J. P., Waters B., Schiebel D., Young W., Golap K., 2007, in Shaw R. A., Hill F., Bell D. J., eds, ASP Conf. Ser. Vol. 376, Astronomical Data Analysis Software and Systems XVI. Astron. Soc. Pac., San Francisco, p. 127
Miotello A., Kamp I., Birnstiel T., Cleeves L. C., Kataoka A., 2023, in Inutsuka S., Aikawa Y., Muto T., Tomida K., Tamura M., eds, ASP Conf. Ser. Vol. 534, Protostars and Planets VII. Astron. Soc. Pac., San Francisco, p. 501
Pascucci I. et al., 2016, ApJ, 831, 125
Pecaut M. J., Mamajek E. E., 2013, ApJS, 208, 9
Pecaut M. J., Mamajek E. E., Bubar E. J., 2012, ApJ, 746, 154
Pinilla P., 2022, Eur. Phys. J. Plus, 137, 1206
Pinilla P., Birnstiel T., Benisty M., Ricci L., Natta A., Dullemond C. P., Dominik C., Testi L., 2013, A&A, 554, A95
Pinilla P., Pascucci I., Marino S., 2020, A&A, 635, A105
Qiao L., Haworth T. J., Sellek A. D., Ali A. A., 2022, MNRAS, 512, 3788
Ratzenböck S., Großschedl J. E., Möller T., Alves J., Bomze I., Meingast S., 2023a, A&A, 677, A59
Ratzenböck S. et al., 2023b, A&A, 678, A71
Ricci L., Testi L., Natta A., Neri R., Cabrit S., Herczeg G. J., 2010, A&A, 512, A15
Rosotti G. P., Booth R. A., Tazzari M., Clarke C., Lodato G., Testi L., 2019, MNRAS, 486, L63
Sellek A. D., Booth R. A., Clarke C. J., 2020, MNRAS, 492, 1279
Shakura N. I., Sunyaev R. A., 1973, A&A, 24, 337
Sierra A. et al., 2024, ApJ, 974, 306
Stadler J., Gárate M., Pinilla P., Lenz C., Dullemond C. P., Birnstiel T., Stammler S. M., 2022, A&A, 668, A104
Stammler S. M., Birnstiel T., 2022, ApJ, 935, 35
Tazzari M., Beaujean F., Testi L., 2018, MNRAS, 476, 4527
van Terwisga S. E., Hacar A., 2023, A&A, 673, L2
van Terwisga S. E. et al., 2020, A&A, 640, A27
Toci C., Rosotti G., Lodato G., Testi L., Trapman L., 2021, MNRAS, 507, 818
Trapman L., Facchini S., Hogerheijde M. R., van Dishoeck E. F., Bruderer S., 2019, A&A, 629, A79
Trapman L., Rosotti G., Zhang K., Tabone B., 2023, ApJ, 954, 41
Trapman L. et al., 2025a, ApJ, 989, 5
Trapman L. et al., 2025b, ApJ, 989, 10
Tripathi A., Andrews S. M., Birnstiel T., Wilner D. J., 2017, ApJ, 845, 44
van der Marel N., Pinilla P., 2023, preprint (arXiv:2310.09077)
Valencia D., Moro-Martin A., Teske J., 2025, preprint (arXiv:2505.09754)
Vioque M. et al., 2025, ApJ, 989, 9

Virtanen P. et al., 2020, Nat. Methods, 17, 261
Winn J. N., Fabrycky D. C., 2015, ARA&A, 53, 409
Zhang K. et al., 2025, ApJ, 989, 1
Zhang S., Kalscheur M., Long F., Zhang K., Long D. E., Bergin E. A., Zhu Z., Trapman L., 2023, ApJ, 952, 108
Zormpas A., Birnstiel T., Rosotti G. P., Andrews S. M., 2022, A&A, 661, A66

SUPPORTING INFORMATION

Supplementary data are available at *MNRAS* online.

UppScoDisks_resolved.dat
UppScoDisks_unresolved.dat
Please note: Oxford University Press is not responsible for the content or functionality of any supporting materials supplied by the authors. Any queries (other than missing material) should be directed to the corresponding author for the article.

APPENDIX A: TABLES WITH DISC PROPERTIES

Tables A1 and A2 summarize the main properties of the resolved and unresolved discs in UpperSco analysed in this study. The complete machine-readable tables are available in zenodo at https://doi.org/10.5281/zenodo.17182603.

Table A1. Properties of resolved discs. The complete machine-readable table is available at https://doi.org/10.5281/zenodo.17182603.

Name	Group Name	SpT	d [pc]	$M_\star$ [$M_\odot$]	$L_\star$ [$L_\odot$]	F_{UV} [G_0]	dRa ["]	dDec [arcsec]	i[°]	PA[°]	Flux [mJy]	R_{90} [arcsec]	R_{68} [arcsec]
2MASS J16042165 2130284	delta sco	K2	144.6	1.05 ± 0.07	0.52	$24.56^{+11.16}_{-9.55}$	0.20	0.41	$11.90^{+0.15}_{-0.18}$	$141.34^{+0.44}_{-0.72}$	$223.30^{+0.52}_{-0.45}$	$0.766^{+0.001}_{-0.001}$	$0.672^{+0.001}_{-0.001}$

Table A2. Properties of the unresolved discs. The complete machine-readable table is available at https://doi.org/10.5281/zenodo.17182603.

Name	Group name	SpT	d [pc]	$M_\star$ [$M_\odot$]	$L_\star$ [$L_\odot$]	F_{UV} [G_0]	dRa [arcsec]	dDec [arcsec]	Flux [mJy]
2MASS J15540240 2254587	delta sco	M4.5	141.9	0.11 ± 0.06	0.03	$9.97^{+1.51}_{-1.31}$	$-0.03^{+0.02}_{-0.01}$	$-0.02^{+0.01}_{-0.01}$	1.95 ± 0.2

APPENDIX B: COMPLEMENTARY FIGURES

In this appendix, we include several complementary figures to the main paper.

(i) Fig. B1 compares the the disc geometry, sizes, and fluxes in this work to values reported in J. M. Carpenter et al. (2025) for the dust continuum emission (dots) and from Zagaria et al. (in preparation) for CO emission (crosses).

(ii) Fig. B2 shows the dust density distribution after 1 Myr of evolution for discs around a 1.0 $M_\odot$, assuming $F_{UV} = 10G_0$ and different type of pressure traps in the models.

(iii) Fig. B3 shows the evolution of the millimetre flux, R_{90}, R_{CO}, and R_{CO}/R_{90} for different values of F_{UV}, and for different pressure traps. These results correspond to the models of discs around a 1.0 $M_\odot$ star.

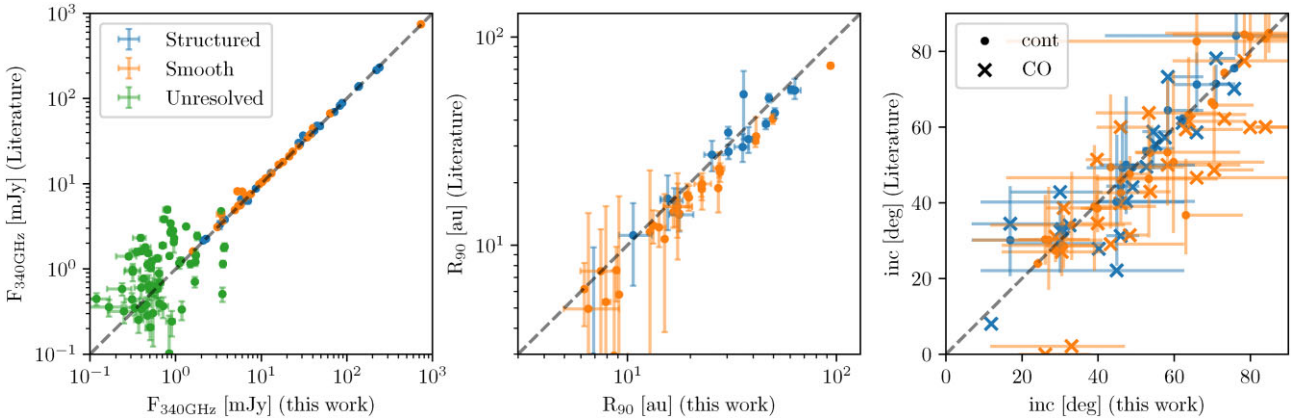

Figure B1. Comparison of the disc geometry, sizes, and fluxes in this work with literature values. From left to right: Dust continuum fluxes, dust continuum radius (R_{90}), and disc inclination. Dot points come from the values obtained from the continuum observations reported in Carpenter et al. (2025), while crosses are from CO estimations from Zagaria et al. (in preparation).

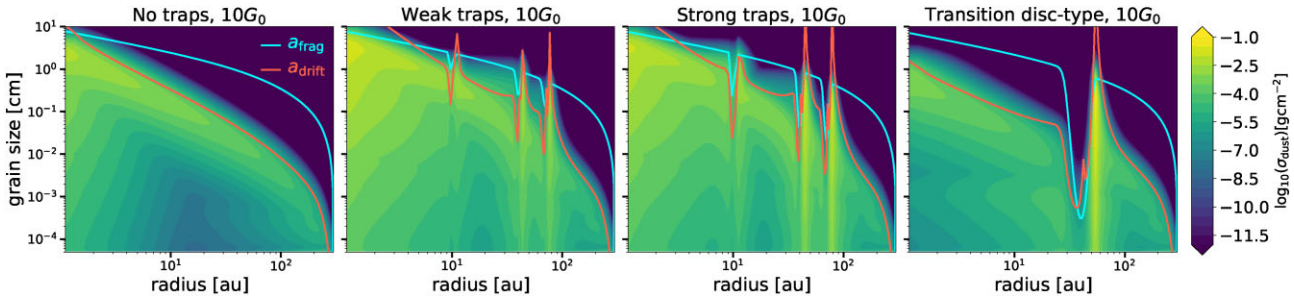

Figure B2. Dust density distribution after 2 Myr of evolution for discs with (from left to right): no traps, weak traps, strong-traps, and transition disc-type trap. All of these models assume a $F_{UV} = 10\,G_0$. These models are for the case of discs around a 1.0 $M_\odot$.

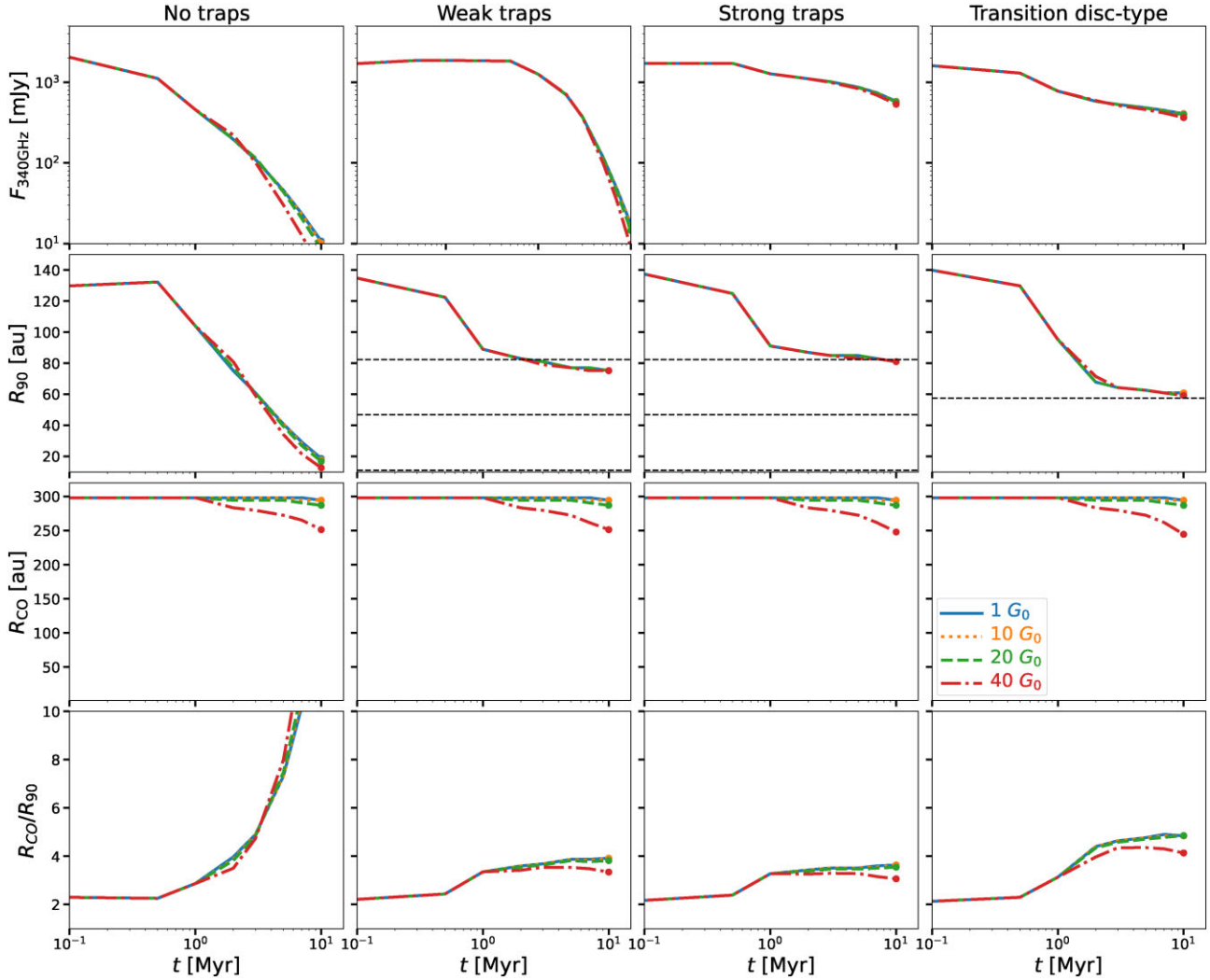

Figure B3. From top to bottom: evolution of the millimetre flux, R_{90}, R_{CO}, and R_{CO}/R_{90} for different values of G_0. From left to right: no traps, weak traps, strong-traps, and transition disc-type trap. These results correspond to the models of discs around a 1.0 $M_\odot$ star.

This paper has been typeset from a TEX/LATEX file prepared by the author.